POLITECNICO DI TORINO

Collegio di Ingegneria Energetica e Nucleare

Master of Science in Energy and Nuclear Engineering

Master's degree thesis

"Unveiling cathodic and anodic materials for potassium-based batteries"

Supervisors:

Prof. Federico Bella

Dr. Lucia Fagiolari

Dr. Daniele Versaci

Candidate:

Federico Giraldo

October 2021

Abstract

The impact of society on the climate of our planet is becoming even clearer, starting from our energy demand, which is in constant growth. This energy used to be generated through fossil fuels. Due to the rise in awareness of the repercussions they have on the whole world, a decarbonized energy generation is evidently needed. Renewables are the medium to achieve this goal, although the main challenges to face are their intermittency and unpredictability. Energy storage plays a critical role in smoothing out their variations, with electrochemical energy storage being the main actor in terms of volumetric and gravimetric energy density. Nowadays, lithium-ion batteries (LIBs) owe the largest market share. However, the high cost and environmentally concerning production hamper their deployment as stationary electricity storage systems. In this context, potassium represents an encouraging alternative, that witnessed exponential interest growth over the last few years. Its chemical and physical similarity to lithium addressed potassium, which exploits the same rocking-chair working mechanism, as a possible substitute in specific applications. K^+/K redox potential *vs.* SHE is -2.93 V, really close to that of Li^+/Li (-3.04 V), suggesting a considerable energy density. Alongside, its natural abundance and low cost, together with the weak Lewis acidity, that allows a fast ionic transport in the electrolyte, outlined a research-worthy solution. However, the bigger ionic radius causes a huge volume expansion in the electrode materials usually employed in potassium-ion batteries (PIBs), with consequent drop of efficiency. Materials that can host the K^+ cation in the intercalation/deintercalation process are needed.

This work is devoted to the study of some electrode materials, through their morphological and electrochemical characterization, and aims to broaden the knowledge around such a new technology. The investigated anode is titanium dioxide, both in the form of nanoparticles and nanotubes, with different lengths, crystalline structures or thicknesses, in order to understand the impact of the nanostructure on the performances. The cathode material studied is Prussian blue in the form of nanoparticles, with different film thicknesses, crucial to enhance the operating voltage and provide stability to the cell in the long term. All the systems were studied employing two different electrolytes, i.e. KPF_6 0.8 M in EC:DEC and KFSI 0.8 M in DME, in T-cell and coin cell configuration. Galvanostatic cycling, cyclic voltammetry, impedance spectroscopy and Mott-Schottky's analysis were carried out as electrochemical tests together with XRD and FESEM for the phase and morphology studies. TiO_2 amorphous nanotubes

showed very good cycling stability in KFSI, delivering 40 µAh cm^{-2}, with a Coulombic efficiency of 97.8%, after 200 cycles. Conversely, the anatase nanotubular structure was not able to deliver a decent capacity, which was attributed to the difficult insertion of large-sized K$^+$ ions in the tight lattice. KFSI-based system was proved to be the best electrolyte in terms of reversibility and cycling stability (CE close to 100%), ascribed to the formation of a homogeneous and robust inorganic SEI layer able to prevent excessive electrolyte/electrode reaction. Despite imide-based electrolytes were reported to cause corrosion issues on aluminium current collectors, Prussian blue thickness of 200 µm was able to provide adequate protection and deliver 20 mAh g^{-1} after 2350 cycles at an operating voltage of approximately 3.2 V. This result is important because aluminium is cheaper and lighter than copper, which is commonly used in LIBs due to the alloy reaction prevention.

List of contents

List of abbreviations

AC	Alternate Current
C_C	Charge capacity
C_D	Discharge capacity
CE	Coulombic Efficiency
CV	Cyclic Voltammetry
DC	Direct Current
DEGDME	Diethylene Glycol Dimethyl Ether
DMC	Dimethyl Carbonate
DME	Dimethyl Ether
EC:DEC	Ethylene Carbonate:Diethyl Carbonate
EDX	Energy-Dispersive X-ray Analysis
EIS	Electrochemical Impedance Spectroscopy
FE-SEM	Field Emission Scanning Electron Microscopy
GC	Galvanostatic Cycling
HCF	Hexacyanoferrate
KFSI	Potassium bis(fluorosulfonyl)imide
KPF_6	Potassium hexafluorophosphate
KTFSI	Potassium bis(trifluoromethanesulfonyl)mide
LIB	Lithium-Ion Battery
MS	Mott-Schottky
NPs	Nanoparticles
NTs	Nanotubes
OCV	Open Circuit Voltage
PB(A)	Prussian Blue (Analogues)
PC	Propylene Carbonate
PIB	Potassium-Ion Battery
RES	Renewable Energy Sources
SEI	Solid Electrolyte Interphase
SHE	Standard Hydrogen Electrode
SIB	Sodium-Ion Battery
SPEIS	Staircase Potentiostatic Electrochemical Impedance Spectroscopy
XRD	X-ray Diffraction

List of figures

List of tables

1 Introduction

The technological development occurred in the last century deeply impacted our society and our way of living, providing countless innovations that improved the global quality of life. Besides, it also provided the instruments necessary to understand the consequences caused on the climate of our planet, and to actively try to remedy for the damages that are going to affect the whole world. It is becoming clearer that the brakeless consumption of depletable resources, especially fossil fuels, has hurt almost irreparably the ecosystems of the Earth. In order to, at least, mitigate the repercussions, we need to take a step forward immediately.

It is evidently difficult to quantify the world emissions that cause global warming, because of the lack of accordance between entities. It is even more difficult to subdivide emissions by sector, in order to implement aimed and effective policies. However, the power sector is known to be the larger contributor, and the CO_2 emissions related to electricity and heat generation were estimated at 39% of the world total [1]. It is clear that, in order to reduce this huge footprint, innovation needs to lead this sector Figure 1.1. Coal power plants account for the large majority and caused 0.3 °C out of the 1 °C increase in global average temperature with respect to pre-industrial levels [2].
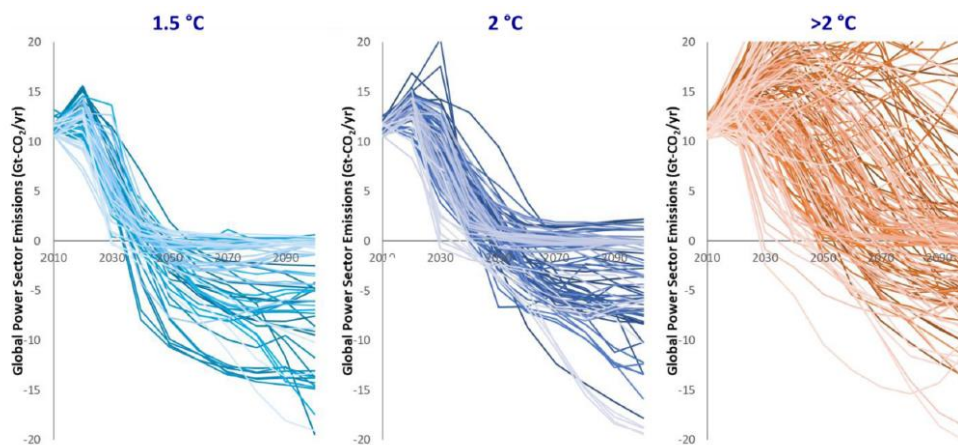
Figure 1.1: Global power sector emissions per year, in three different scenarios, reaching different warming levels. Each line represents a different model from IPCC database [3].

What emerges from Figure 1.1 is that the carbon emissions from power plants in almost every model become negative from about 2030 on. It is because of the compulsory employment of carbon dioxide removal (CDR) technologies, of which the large-scale deployment was demonstrated to help reducing the costs of the energy transition and decarbonisation [4]. Indeed, the substitution with carbon-free power generation technologies will not solve the global warming alone. The CO_2 trapped in the atmosphere will keep on heating the planet due to the greenhouse effect and a related concatenation of events that already started. Moreover, especially in the beginning of the energy transition, the employment of cheap, fast-response and low-carbon gas turbines will significantly contribute to a containment of the electricity price escalation Figure 1.2. Their coupling with direct carbon-sequestration technologies will play a role even in the employment of these systems after the shutdown of last coal plant.
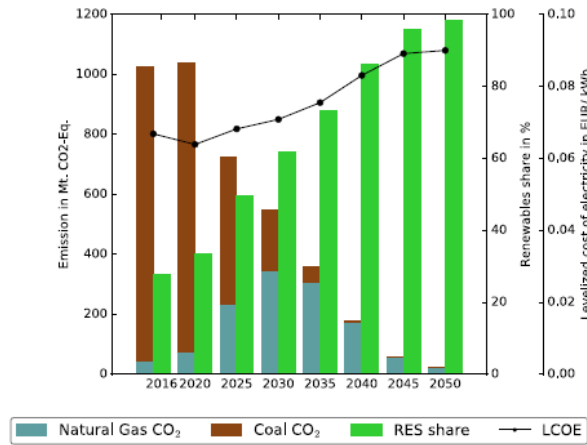
Figure 1.2: Total EU emissions and renewable penetration in the power sector, today and growth trends modelled [5].

1.1 Towards a zero carbon-emission scenario

Today, the electricity generation is completely centralized around big plants, mostly coal Figure 1.2, from which departs through interconnected networks until it reaches the consumer. Renewable generation involves the deployment of many de-centralized smaller power production areas closer to consumers, but largely cross-linked in order to exchange electricity each other. The large employment of renewable-based power sources, such as wind, solar,

hydro could technically accomplish the task of switching towards a sustainable power generation. The main issue is, indeed, the management of such an unpredictable and hardly-controllable system that requires the creation of a completely new grid infrastructure. Additionally, the deeper the penetration of variable renewables (VRE), the harder the challenges we are called to face and the larger the cost of implementation [6].

The paradigm of energy consumption today is based on the production adjustment aimed to meet and satisfy the demand. This mono-directional adaptation assumes an energy generation that is controllable and can be increased or reduced arbitrarily. Anyhow, this flexibility cannot be guaranteed in an energy mix where wind and solar power are the main contributors. Because of their weather-dependency, the production will be no longer tailored on the consumption. It is the latter that needs to be reshaped on the energy availability. The electrification of final uses, such as buildings heating and transportation, is required to change the load shape on the power grid and is compulsory in every net-zero-carbon scenario [3]. It will certainly increase the energy demand, but nevertheless the flexibility will be enhanced. Demand responsive (DR) control systems are under development in order to facilitate renewable integration at higher penetration rates. In a VRE-based power system, instead of reducing the peak demand, this system targets the instantaneous consumption though signals sent to the customers by utilities. These signals are aimed to generate an automatized response based on the energy readiness, increasing or reducing the consumption [7]. Electric vehicles, for instance, are parked most of the time. Through a proper parking infrastructure they could help balancing supply and demand, being charged during excess of production and discharged during shortages. This sort of instant power modulation is not supposed to significantly affect the final users because it will be employed as fast-response short-time system [8]. In this way, the vehicle will still have enough charge to be driven when required. Moreover, the cost intensity of electric vehicles to consumers is expected to decrease, since these operations as ancillary[1] service will be rewarded.

Variability of renewables is spatial, further than temporal, with large diversity that can cross regions. Therefore, another step forward a de-carbonised power system is the expansion of existing networks at a continental scale in order to smooth out these local variations. Since fluctuations are experienced also on a seasonal and hemispherical basis, eventually the network expansion will involve the interconnection of continent-size supergrids. In Europe alone, in

---

[1] They are defined as the services, integrated in the transmission line, needed to contribute to its dynamic stability and to maintain the quality of the electric power, namely in terms of voltage and frequency.

order to meet the zero-carbon emission targets by 2050, the interconnection capacity of the transmission grid between nations should expand at least 4 times with respect to 2016 levels (from 79.5 GW to 362 GW [5]). It will require massive investments, and authors accounted for the transmission grid only, without including the distribution grid ampliation to access local renewables Figure 1.3.
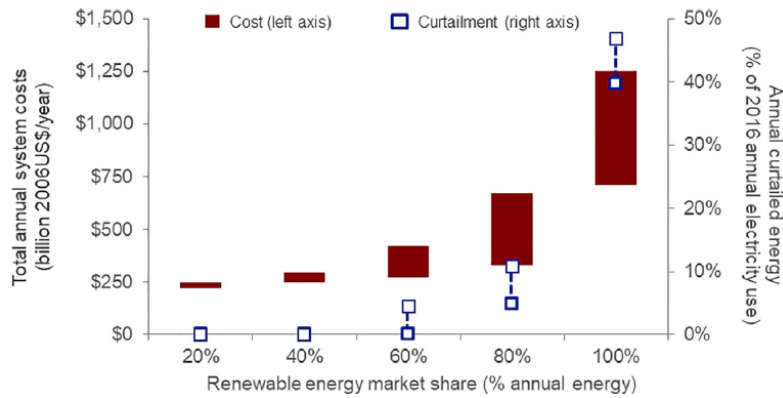
Figure 1.3: Non-linear increase in system cost and curtailment of electricity (wind and PV) with respect to the renewable penetration [6].

An important indicator emerging from this graph is the exponential increase of curtailed energy as the renewable penetration deepens. Curtailment is defined as the amount of power that can be potentially produced instantaneously, but it is not due to technical reasons that can space from lack of demand, minimum operational levels of some power plants, network congestion or economical non-convenience [9]. It is intended as a loss due to the missed production, representing a critical aspect of system with higher RES share. Curtailed energy non-linear increase is justified by the need of deploying additional power than what effectively needed; typically, it is distributed in large spatial areas to smooth out local fluctuations, in order to always have a statistical minimum production. Including sources of flexibility in the grid allows to reduce curtailed energy by reducing the additional unused power deployed. Storage availability is the most efficient solution to prevent this energy waste. From a quantitative perspective, in [10] it was proven that, in California, achieving a 72% CO_2 reduction through RES deployment led to a 30% of power curtailment. On the other hand, storage implementation allowed 90% of CO_2 reduction and 9% of curtailment even though the same renewable penetration was employed.

1.2 The role of storage

In a low-carbon VRE-dominated power network is obviously fundamental being able to store the electricity, as well as to supply, whenever a shortage of production occurs. The main tasks to accomplish are the peak-shaving and the frequency regulation: the difference lies in the response time, that could be in the order of hours, minutes or seconds. In this optic, it is critical to distinguish between energy storage and power storage, with the former being dominant in nowadays market share. Bulk storage is typically performed by pumped hydro (PHES). In fact, it was originally designed to help baseload coal plants, which were not able to rapidly ramp up their production during peak hours. Compressed-air (CAES) is the other bulk storage system that prevails the market. Air is compressed when excess of production starts to be experienced from the grid. It is then blended with fuel and driven into a gas turbine when the demand rises again without being satisfied. Emission reduction achieved by this technology is up to 60% with respect to a single-stage gas turbine [11]. Such a system, requiring large underground caves to store high-pressure air, suffers the same limitation of PHES: geographical constraints, that hamper their large-scale deployment and force the creation of big storage facilities. Due to this reason, these assets are generally far from consumption centres, loading the small-distribution grid and experiencing considerable transmission losses. Additionally, the response time is, at best, in the order of 15 min. It was perfectly coupled to dispatchable systems, like fossil fuel power plants, but cannot take up the challenge addressed by the rapid variability of RES.

Frequency control is intended as the rapid delivery of large amounts of power when needed, that in fact prevents the frequency of the grid to drop. Distributed power storage was designed on this purpose. Its strength is the fast response and contained size, that permits the on-site employment closer to the users. The outcome is to reduce by 40% the amount of energy needed to regulate the frequency if fossil fuel plants were employed on this task [12]. The peak evolution of this technology is to place energy storage devices at a neighbourhood-level, to control the voltage directly at the customer feeder. Coupled to local generation, this solution will help balancing the grid without overloading the distribution network. The ensemble of the storage device and all the power electronics, comprising transformers and inverters, is usually defined Community Energy Storage (CES) [13].

Batteries would fulfil the storage requirement, given a massive decrease in their employment cost, which is still quite high. Interest arose around such a technology in the past few years. The

round-trip efficiency, which prevents energy waste, is outstanding with respect to other solutions [14]: the modularity allows the implementation from the household-size up to battery parks capable of feeding cities; the quick response time suggests a possible employment in the full range of storage needs, from frequency control to load-shifting and congestion relief. Because of these unique features, there are many potentialities for battery employment in a deeply decarbonised power grid Figure 1.4, given an adequate cost adaptation.
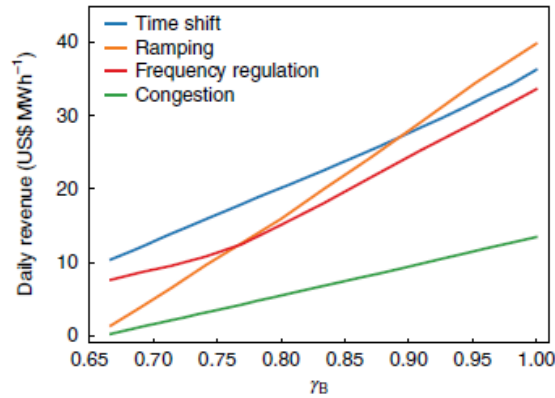
Figure 1.4: Revenues trend *vs*. battery efficiency in different operational modes [14].

1.3 Rocking-chair batteries

Portable electronics is the marked sector that pushed the development and penetration of batteries around the globe in the past years. Due to their extremely high energy density, cycling reliability and fast response, lithium-ion (LIBs) batteries dominated this sector and drove the research studies forward a deeper optimization. The sudden increase of devices demand and the diffusion of electric vehicles raised consistently the lithium consumption. Following its global scarcity, LIBs cost grew exponentially, clearing the need to develop a new electricity storage technology. In order to exploit the know-how gained over years, sodium-based batteries have been thought as possible substitutes, having similar chemical and physical characteristics, further than being much more abundant on earth. However, the large Na^+ radius, resulting in structural alterations and capacity decay, the lower operational voltage and the smaller ionic conductivity, hindered further development [15]. Potassium-based batteries have been recently discovered as research-worthy alternative Figure 1.5, because they exploit the same rocking-

chair mechanism Figure 1.6 of the abovementioned: during discharge, the cations de-intercalate from the anode (high-energy state), move through the electrolyte and intercalate into the cathode (low-energy-state). This generates uneven charge distribution with positive accumulation that drives an electron flow in the external circuit to balance the charge, coming from the oxidation/reduction couples at the electrodes. During the charging phase, electron flow is reversed. Cations are deintercalated from the cathode and driven to the anode, where they are hosted. The name of this mechanism derivers from the cations, which move back and forth between the electrodes.
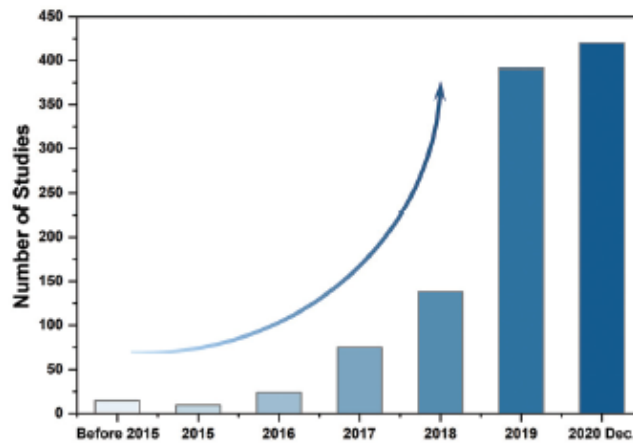
Figure 1.5: Number of publications on PIB according to Web of Science, showing recent exponential-rising interest [16].
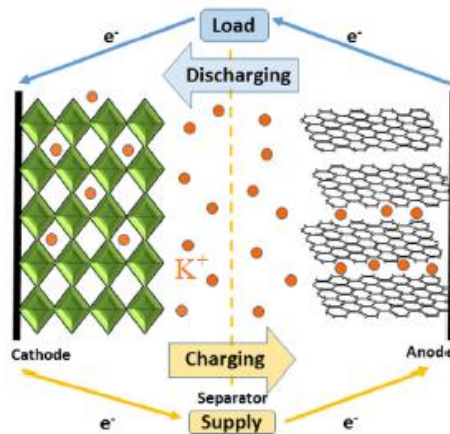
Figure 1.6: General scheme of a rocking-chair potassium-ion battery.
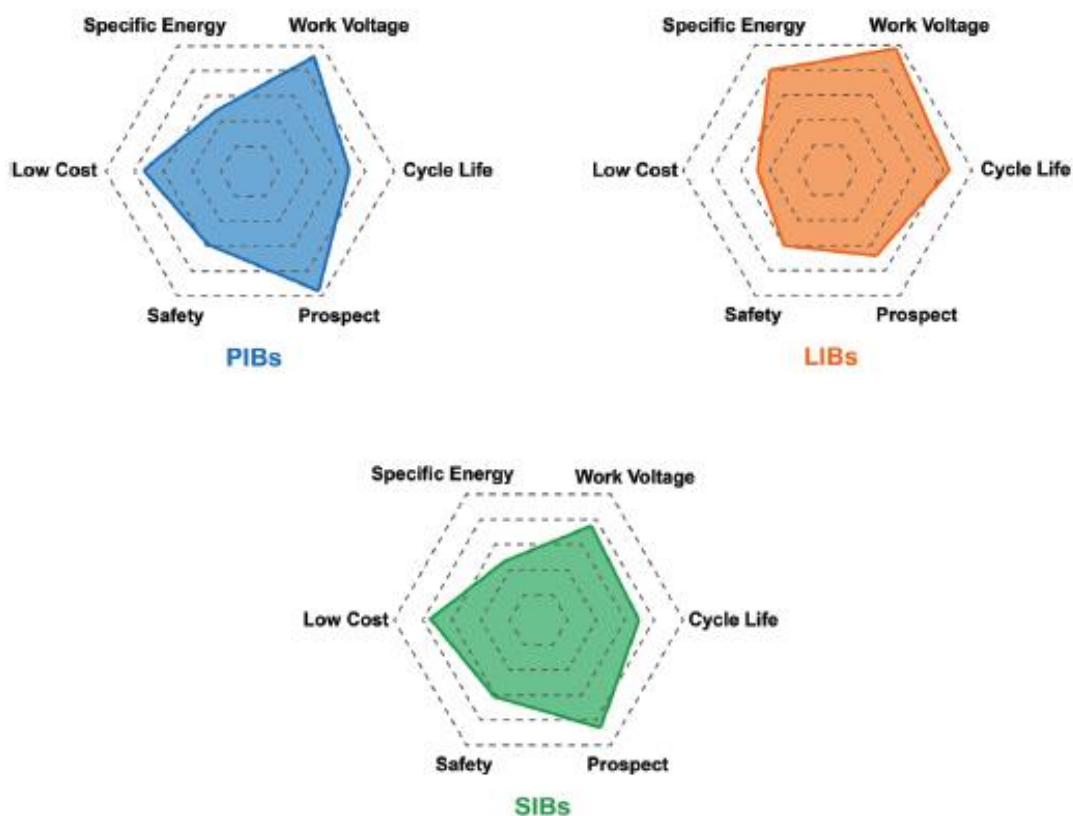
Figure 1.7: Qualitative comparison of some relevant properties among alkali-earth batteries.

A qualitative Figure 1.7 and quantitative Table 1.1 comparison between batteries based on this technology is herein reported. Analysing Table 1.1, it could be understood why potassium gained interest over sodium: 1) it shows a more negative standard potential (0.2 V higher) *vs*. SHE, closer to lithium, guaranteeing higher operational voltage and energy density; 2) potassium can form stable graphite intercalation compounds (GIC), which was not possible with sodium, allowing to exploit the knowledge acquired with lithium and the high specific capacity of graphite; 3) the weaker Lewis acidity provided by the smaller charge density of potassium gives it the smaller de-solvation energy and Stokes' radius in liquid electrolytes. They result in higher ionic conductivity and faster diffusion at electrode/electrolyte interface [16, 17]. These features promise good reaction kinetics and better rate capability compared to other alkaline-earth-based batteries. Additionally, the lower melting temperature can result in

local self-healing from dendrites[2] due to Joule effect [17]. Furthermore, potassium does not alloy with aluminium, enabling aluminium employment as current collector rather than the usual more expensive and heavier copper. With the scope of cost and weight containment, this last feature is crucial.

On the drawback side [18], the much larger ionic radius of K^+ could decrease its mobility in bulk host material and lead to big volume variations during cycling. It may result in structural damages and, ultimately, poor cycling stability. The lower Lewis acidity may lead also to a weaker and more fragile SEI layer and hamper potassium-metal anode development. Furthermore, the high reactivity of K^+ to oxidation when exposed to air shows a critical safety issue that must be solved before a large-scale application.

A final comparison with lithium helps in clarifying the application of this new technology. It is evident that no competition could exist in terms of portable devices and electric vehicles due to the much larger weight of potassium, that dwarfs its energy density. Conversely, under a stationary point of view, the excessive cost of lithium cannot accommodate the electricity storage demand deriving from an increasing renewables penetration. Since the weight is not a relevant issue for such an application, this is the final aim of PIBs [19]. Alongside, a promisingly-long cycle life could become a relevant deciding factor. The aforementioned issues in potassium employment witness the necessity of new electrode materials development to fully harness the potential of this technology.

---

[2] Complex process during plating, resulting in uneven metal deposition as spikes on the electrode surface. Their growth during cycling may end up in separator puncturing and consequent short circuit.

Table 1.1: Physical and chemical properties comparison between the alkaline-earth metals [16].

Properties	Lithium	Sodium	Potassium
Atomic number	3	11	19
Earth crust abundance [wt.%]	0.0017	2.3	1.5
Concentration in seawater [mg L^{-1}]	0.1	10,556	380
Density [g cm^{-3}]	0.535	0.968	0.856
Melting point [°C]	180.5	97.7	63.4
E^0 *vs.* SHE [V]	-3.04	-2.71	-2.93
Stokes radius in PC [Å]	4.8	4.6	3.6
De-solvation energy in EC [kJ mol^{-1}]	208.9	152.8	114.6
Ionic conductivity in 1M in xPF_6 in EC/DEC [mS cm^{-1}]	4.38	6.38	6.55
Ionic conductivity in 1M in xFSI in DME [mS cm^{-1}]	16.9	16	13.1
Theoretical capacity [mAh g^{-1}]	3827	1165	685
Cost of industrial grade metal [kUS$ ton^{-1}]	100	3	13

2 Potassium-ion batteries

A battery is a device that transforms reversibly (if rechargeable, i.e. a secondary battery) the chemical energy of a reduction/oxidation reaction occurring at its electrodes in electrical energy. It is composed of a stack of single cells where reactions take place. The main components are a cathode, that accepts electrons hosting the reduction reaction during the discharge phase, an anode, that provides electrons hosting the oxidation reaction, and an electrolyte, that permits the motion of ions (charge transfer), but not of electrons, preventing the short circuit between electrodes [15]. More specifically, PIB working principle is the previously explained, also named "rocking chair" mechanism Figure 1.6, in which the capability of the electrode structure to host K+ ions is the critical step. It is referred to as intercalation if the structure is layered with free space for ions accommodation among planes, or insertion if the structure is three-dimensional with cavities and narrow channels to connect them.

In the forthcoming paragraphs, the state-of-the-art of PIBs is reported.

2.1 Anode materials

The anode is responsible to store ions in a high energy state. It enhances the operating voltage of the cell and, consequently, its energy density. It must provide chemical stability when in contact with the electrolyte because, otherwise, its continuous decomposition may happen. Pure metal is generally considered the best anode because it provides the highest possible energy state and it is able to host the highest number of ions per unit volume [20]. However, along with these advantages, several drawbacks that practically hamper its use emerge: the high reactivity coming from the highly electronegative reduction potential and the dendrites growth on the surface. These issues have been already experienced in LIBs and are expected to occur even more largely in PIBs, being it even more reactive than lithium. Employing other materials to reversibly store ions, as well as increasing battery safety, is the research focus that led to the investigation of other anodic materials Figure 2.1.

Figure 2.1: Voltage windows *vs*. specific capacities for PIB most common anodes.

2.1.1 Carbon intercalation anodes

Graphite has been intensively employed and studied as anode material in LIBs because of its abundance, dendrite formation prevention and because it is a natural electronic conductor. Hence, due to the chemical similarity between lithium and potassium, it is one of the best candidates to solve the anodic functions. The theoretical capacity in PIB has been determined as about 279 mAh g^{-1} (for LIB it is 372 mAh g^{-1}), but the main challenge is given by structural damages issued by continuous large-radius K$^+$ (de-)insertion. Commercial expanded graphite has been investigated because of the larger space between planes to accommodate ion intercalation, showing good rate performances of about 170 mAh g^{-1} [21] and an improvement of the diffusion coefficient. Graphitic carbon cations storage is characterized by an intercalation mechanism, with the formation of stable intermediate compounds (KC$_x$, where x is equal to 8, 24 or 36) associated with carbon layer expansion. Some deeper investigations suggest that the formation enthalpy of those carbon-potassium compounds is lower than in LIB, indicating a more spontaneous reaction [22].

Non-graphitic carbons with different microstructures have also been objects of research. Still, the main threat for their use is represented by structural alterations, which were initially faced through intensively N- and F-doping, revealing promising capacities of about 350 mAh g^{-1} [23]. Larger space between planes might contribute to a faster intercalation process, enhancing reaction kinetics and increasing the diffusion coefficient. Although the notable rate capacity

provided by these carbonaceous materials, it has been demonstrated that they are not able to reach the bulk energy density of graphitic carbons; yet, their lower production cost from wastes and the eco-friendliness can contribute to their employment [24].

2.1.2 Alloying anodes

These electrodes exploit the properties of some elements that belong to groups 14 and 15 (such as Sn, P, As, Sb, Bi) to alloy with potassium. Alloys can be reversibly formed during charge/discharge process, accommodating a larger number of K^+ ions than intercalation-type anodes. Potassiation reaction generally occurs via successive steps that contribute to a multi-plateau discharge curve, but the volume changes issued by such a deep modification are so relevant that electrode pulverization is very likely to occur. The reaction is described below (2.1), where M is the alloying metal and K is potassium, while n is the electron transfer number.

$$xM + nK + ne^- \rightarrow K_nM_x \qquad (2.1)$$

Tin nanoparticles showed a capacity of about 197 mAh g^{-1} [25] with a two-step alloying process. A 3D tailored nanostructure with carbon coating [26] proved to help integrity during repeated cycling, drawing the research direction for this technology. It was exploited also to manage the impressive volume expansion of Sb-based electrodes (more than 300%) with initial successful results, embedding nanoparticles in a graphene skeleton and delivering a capacity of about 474 mAh g^{-1} [27]. Antimony alloys with K throughout a three-step process, with a molar ratio of about 1:3. The high electron transfer number gives rise to the reversible capacity characteristic of these electrodes, despite the cycling stability is much lower than what observed in LIBs and SIBs. Alloying anodes high density makes them also more suitable than carbonaceous electrodes, since in a stationary application the volume is a major concern than the weight.

2.1.3 Conversion anodes

Conversion is a mechanism that, generally, exploits the reduction of oxides to their metallic state, creating new chemical compounds with a completely different structure . It is also possible for the so-formed metal species to give rise to a reversible alloying process that

enhances the capacity of the material. In the reaction formula reported in (2.2) [28], M is the transition metal (Fe, Co, Mo, …), A is the anion (O, S, …), n is the anion oxidation state.

$$M_xA_y + (yn)K^+ + (yn)e^- \rightarrow xM + yK_nA \qquad (2.2)$$
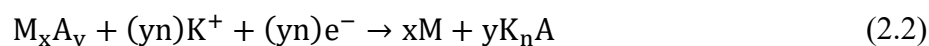
A relevant volumetric expansion is here present, posing serious challenges to the employment of these material family. Moreover, the chemical alterations of the electrode lead to poor conductivity and remarkable voltage hysteresis[3]. Conversely, the number of electrons involved is larger than alloying anodes, proving the reversibility of the reaction, while the reduction state of the transition metal to the metallic state provides theoretical capacities larger than intercalation anodes.

CuO nanoplates were employed as conversion anode, resulting in a reversible capacity of about 342 mAh g^{-1} and showing good cycling stability at 200 mA g^{-1} [29]. The first potassiation resulted in the conversion from CuO to KCuO and Cu. Cu nanoparticles were reversibly reoxidized to Cu_2O during the successive charging phases. Because of the tailored nanostructure, the deposited electrode was really thin, partially solving the poor K^+ diffusion by means of a shorter path. Metal sulphides enhanced the electrical conductivity and reactivity, despite the latter also drove undesired side reactions. These challenges, faced through carbon-based composites, led to the achievement of an impressive capacity of 679 mAh g^{-1} by stabilizing MoS_2 with reduced graphene oxide (rGO).

2.1.4 Na-K anodes

This technology gained interest recently because aims to exploit the good properties of pure potassium metal while trying to tackle some of its criticisms. The interface between anode and electrolyte is a pivotal point due to the occurrence of reactions that can be unstable or show dendrites growth. However, dendrites cannot form on a liquid/liquid anode/electrolyte interface, enabling safer battery operation. Molten anodes generally require high operating temperatures, larger than 300 °C, representing a hard challenge in terms of thermal management and corrosion. In [30], a liquid K-Na anode was investigated due to the eutectic below room temperature. This anode (33.7 wt% Na) was absorbed onto a porous carbon substrate in order

---

[3] Voltage hysteresis: analysing charge-discharge curves they are generally not overlapped, with distance between them depending on irreversibilities, residual polarization and charge transfer impedance [44].

to stabilize the interface with the separator, as well as to produce electrodes with the desired shape. KNC (K-Na-C) delivered good cycling stability over 400 cycles at 120 mAh g^{-1} and prevented dendrites growth in contact with the organic electrolyte. It is worth noticing the complete recyclability of such an electrode, because, when immersed in tetraethylene glycol dimethyl ether (TEGDME) solvent, the floating alloy is completely expelled from the sinking carbon matrix

2.1.5 Other intercalation anodes

This section groups all the other materials that rely on the intercalation process to store potassium cations, without being carbonaceous. Titanium-based materials are one of the most common solutions, based on the Ti^{4+}/Ti^{3+} redox couple. The discharge capacity typical of this family is relatively low but revealed its attractivity analysing the stability over repeated (de-)insertions; it suggests a very good strain resistance of the structure coming from the controlled volume expansion. Due to the semiconductor properties, a conductive carbon inclusion in the mixture is beneficial to improve the electronic conductivity. Interest was gained also by the ability of sustaining a wide range of current densities, i.e. showing very good stability at low cycling rates (97 mAh g^{-1} at 30 mA g^{-1}), as well as undergoing fast cycling up to 15C. These results are shown in [31] for K$_2$Ti$_4$O$_9$, but it was reported that a tailored nanostructure with improved crystal plane spacing and an open-porous network could reach capacities of 151 mAh g^{-1} at 50 mA g^{-1}. Thus, it is clear that an analysis and optimization of the structure, with its pores and intercalation sites, is the key to achieve suitable capacities exploiting the stability of these compounds. Other alkali titanium oxides were objects of research following the results in Na/Li-ion batteries, such as K$_2$Ti$_8$O$_{17}$ and K$_2$Ti$_6$O$_{13}$, obtaining capacities of about 90 mAh g^{-1} after a large initial capacity drop attributed to irreversibility and ions that remain trapped upon cycling [32].
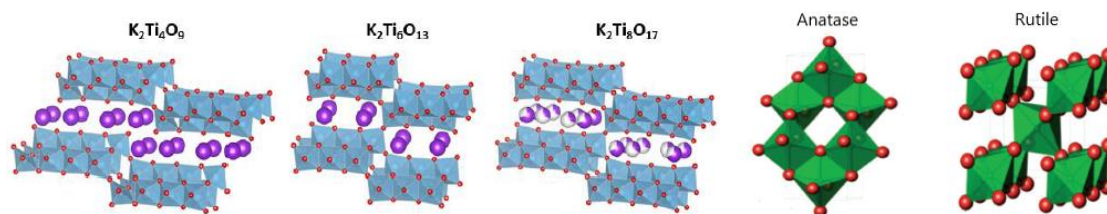
Figure 2.2: Crystal organization of titanium-based compounds revealing planar structure given by TiO_6 octahedra chains and potassium ions (purple) in the space between layers for $K_xTi_yO_z$. On the right side, crystal organization of TiO_2 compounds.

Titanium dioxide polymorphs, namely amorphous, anatase and rutile, are commercially well-known materials with low cost, low toxicity and environmental friendliness, regarded as promising anode materials for SIBs [33], although not widely tested yet in PIBs. The first two are under investigation in this thesis, following the similarity with sodium. Their crystalline structures differ on the way TiO_6 octahedra arrange each other in the lattice. In the amorphous phase, no long-range order can be recognized, forming free spaces to accommodate ions diffusion and stress relaxation to prevent damages coming from ions insertion. Amorphous nanotubes were reported to provide active sites for cations insertion in the interfacial regions. In theory, two reductions per formula can be induced, but practically the second is hampered by the first cation that might be trapped in the structure. This issue can be tackled by designing nanotubes with an appropriate diameter above 80 nm. The anatase phase is the most studied in the SIB field because of its zigzag channels providing suitable ions diffusion pathways. Anatase mesoporous nanoparticles were also tested delivering reversible Na ions storage up to 11000 cycles with capacities of 77 mAh g^{-1} at 20C (1C = 335 mA g^{-1}), suggesting a looser structure in order to efficiently store large ions.

2.2 Cathode materials

The cathode is responsible of determining the energy density of the cell because it fixes the low-energy state towards which ions tend to move during the discharge. The larger the energy difference between the electrodes, the larger the voltage difference and consequently the energy that can be stored by the battery. The cathode should be a good oxidising agent to promote electron motion in the external circuit, while providing a high-enough operating

voltage. The large majority of cathodes are intercalation-type, but research progress lies behind anode development in terms of cycling stability and specific capacity, requiring intense efforts in the upcoming years.
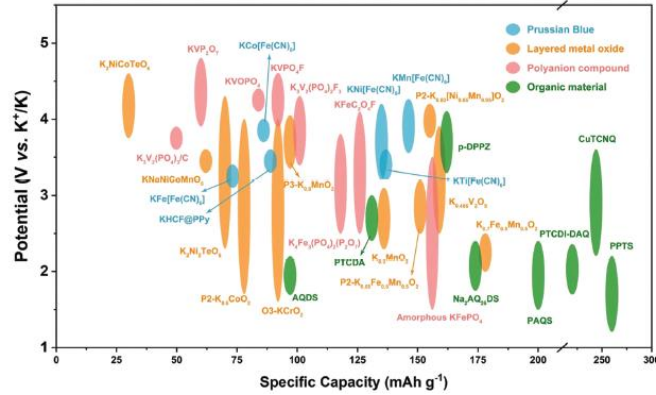
Figure 2.3: Voltage windows *vs*. specific capacities for PIBs most common cathodes [28].

2.2.1 Layered transition-metal oxides

Layered transition metal oxides (TMOs) are used as battery cathodes in LIBs and SIBs and considered promising solutions also for K ions storage because of their high energy density and capacity, coming from the rigid close-packed structure. The general composition is K_xMO_2, where M is typically Fe, Mn, Ni, Co, V, etc. or a mixture of two of these elements. The major challenge is again the massive volume change induced by K^+ cyclic (de-)intercalation, that ends up in the electrode pulverization or sliding between layers, witnessed by a rapid capacity fading [16]. The reaction mechanism involves the insertion of K^+ ions in the open frameworks given by octahedral and prismatic sites:

$$KMO_2 \rightarrow K_{1-x}MO_2 + xK^+ + xe^- \tag{2.3}$$
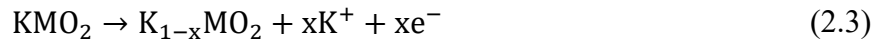
$K_{0.7}Mn_{0.5}Fe_{0.5}O_2$ nanowires were synthetized, providing good specific capacity of about 180 mAh g^{-1}, higher than what was obtained with the corresponding nanoparticles synthesis, and an improved rate capability in repeated cycling. This is attributed by authors to a better and more robust interconnection between layers that enhances potassium kinetics. It was also reported that, from a deeper analysis on the discharge curves of layered TMOs, voltage curves look steeper than those of LIBs and SIBs. It might be caused by larger space between layers

following K^+ insertion. Larger space between oxygens reduces the screening effect on positively charged potassium ions, consequently reducing the total amount that can be stored and increasing the rearrangement undergone by the structure [34]. This issue was not present in Li- or Na-based layered oxides and represents a drawback hard to overcome regarding this technology.

2.2.2 Polyanion compounds

The general structure of this class of materials is $K_xM_y[(XO_4)]_z$, where M is a metal (Fe, V, etc.) and X is P, S, Si, As, Mo, etc. Polyanion compounds are addressed to solve the repulsion issue between alkali cations occurring in layered TMOs. MO_x and (XO_4) polyhedrals promote a better ion storage framework through the screening of the intercalated cations, able to alleviate the volume expansion. Additionally, they are attributed to deliver a high potential up to 4.2 V *vs*. K^+/K, contributing to a noticeably high energy density. However, this high operating voltage points out the requirement of new electrolyte investigation [16]; generally, beyond 4 V, side reactions take place and hamper the safety and reversible operation of the cell. On the drawbacks side, the low tap density of this family of compounds plays an important role because it lowers the volumetric energy density.

In [35], the investigation of $KVPO_4F$ in 1 M KPF_6/EC:PC 1:1 electrolyte resulted in an excellent rate capability in the window 2.0-5.0 V, with a specific capacity of 92 mAh g^{-1} attributed to the V^{4+}/V^{3+} redox pair. This material proved also to withstand prolonged cycling with contained volume shrinkage at 5.0 V (*vs*. K^+/K), attained to 5.8%, one of the lowest values among PIB cathodes. On the other hand, ongoing progressive electrolyte decomposition was verified, as expected, requiring further studies. Noteworthy is that a full cell was also investigated Figure 2.4, employing $KVPO_4F$ as cathode and VPO_4 as anode, with outstanding results in terms of cycling stability. The so-assembled cell achieved an operating voltage of 3.1 V, a specific capacity of 101 mAh g^{-1} (0.5C) and a capacity retention of 86% over 300 cycles. The stability was also assessed at 10C to evaluate the rate capability, achieving 76 mAh g^{-1} (*vs*. cathode) of specific capacity and retention of 86.6% over 2000 cycles [36]. These results are very encouraging and trace the direction for further investigations.
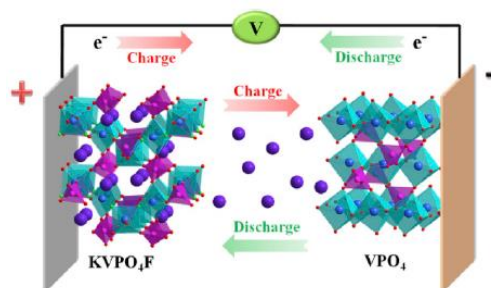
Figure 2.4: Schematic illustration of the full-cell assembled by J. Liao et al. [36], that employs a polyanion compound as cathode and an intercalation non-carbonaceous compound as anode.

2.2.3 Organic cathodes

Organic materials are usually addressed as a possible solution in every alkali-ion technology because of their flexible structure, electrochemical stability, large availability, low price and environmental friendliness. These are all helpful features towards the industrial deployment of low-cost and socially acceptable energy storage solutions. Moreover, intermolecular interactions between organic compounds are generally weaker than that of other materials, therefore large-ion intercalation induces little damage and good kinetics. Nonetheless, a weaker bonding may result in small molecules decomposition, lowering the capacity as cycles proceed [28]. This issue has been successfully tackled in LIBs and SIBs through several techniques, such as polymerization and anchoring. It is worth noticing that organic cathodes lack available potassium sources, therefore either pre-potassiation or metal-containing organic compounds employment is required.

What was already experienced in LIBs and SIBs is the low operating potentials of organic cathodes, generally below 2.5 V, that limits the storable energy and requires larger battery-packs deployment [16]. Poly(pentacenetetronesulphide) (PPTS) was investigated [37] in half-cell configuration, showing surprising results: specific capacity of 260 mAh g^{-1} at 0.1 A g^{-1} and good cycling stability of 190 mAh g^{-1} at 5 A g^{-1} after 3000 cycles. The structural flexibility is addressed to be responsible for the damage prevention and for the fast K$^+$ diffusion that made this solution research-worthy. However, electrochemical tests showed the redox reactions to take place at low voltages of about 1.4 and 2.1 V.

2.2.4 Prussian blue analogues

It is a wide family of material also known as hexacyanoferrates due to the presence of multiple $(CN)^-$ ligands. They provide a rigid cubic structure bonding together transition metals (M_A and M_B), such as Fe, Mn, Ti, Co, etc. with the general formula of $K_x M_A[M_B(CN)_6] \cdot nH_2O$. The number of alkali-ions per structure can vary between 0 and 2, denoting Fe-HCFs as Prussian Green, Prussian Blue and Prussian White, respectively. They also represent the successive phases of ion intercalation. When all the Fe^{II} are oxidized to Fe^{III}, the discharge phase is considered completed and potassium ions are ready to be extracted. Counterions are also responsible for the crystalline phase transitions [38], which is stable in the case of K-ions, but it was not the case for Li ions, given the smaller ionic radius [18]. The holes available can accommodate potassium ions as well as water molecules Figure 2.5, because of the suitable size of the channels. Hence, PBA are generally cheap to be obtained through precipitation methods and subsequent drying, but the industrialization of the process is still not easy. Water may remain trapped in the channels, occupying an active site for K^+ insertion [34], whereas complete dehydration is hard to achieve given the fast kinetics of precipitation. Alongside, forcing water expulsion to free the interstitial spaces might end up damaging the whole structure.

PBA are promising cathode solutions due to their structural rigidity that allows minor volume changes, therefore impressing cycling stability. An open framework responsible for fast kinetics is critical in rate capability enhancement. Besides, the low cost and environmental friendliness of hexacyanoferrates can contribute to the deployment of PIBs.
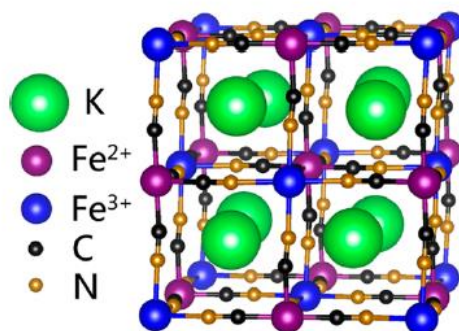
Figure 2.5: Schematic cubic face-centered lattice structure of $K_2 FE^{III}[Fe^{III}(CN)_6]$ showing interstitial cations. Those space can be filled with water molecules reducing the hostable ions [38].

Optimization of the structure passes through the change of redox-center atoms by doping with other transition metals. The best results in terms of storable potassium ions are reported in [39] by the inclusion of Mn atoms, achieving a potassium content of 1.89 over a maximum of 2 per formula. Two voltage plateau were recognised at 3.7 and 3.56 V with a specific capacity of 146 mAh g^{-1} at 0.2C. Iron-based HCF were also synthetized [40] as highly-stable cathode, which exhibited 111 mAh g^{-1} capacity and retention of 80% after 1000 cycles, demonstrating a long-term cyclic reversibility.

Authors in [41] report the characterization of commercial Prussian blue nanoparticles (KPBNPs) in both half-cell and full-cell configuration using a non-aqueous electrolyte. In the former, a capacity of about 73 mAh g^{-1} was obtained and showed a small capacity decay of 0.09% in the first 50 cycles. The role of the interstitial water was investigated too: its presence was unavoidable after the synthesis and negatively affected the performances in the first cycles due to its ongoing decomposition. Therefore, the Coulombic efficiency gradually increased as the electrode dried upon cycling, while the volume change was assessed to a contained 6.9%. In the full-cell configuration, a SuperP commercial anode was employed, following the maturity of carbon-based anodes in LIBs. A stable capacity of 64 mAh g^{-1} at 100 mA g^{-1} was reported after 50 cycles, which is a promising result given the very low cost, sustainability and commercial availability of employed materials.

2.3 Current collector

The role of the current collector is to deliver electrons the closest possible to the active material. The active material is directly deposited on it, therefore mechanical stability, lightness and corrosion resistance should be assured, as well as electrochemical stability in the operating voltage range. The choice of a suitable material lies generally between copper and aluminium Figure 2.6, with the former being usually a better conductor despite being heavier and more expensive. In LIBs, copper is employed as a standard, because it does not alloy with lithium. However, since the beginning of the research on SIBs and PIBs, it was clear that - in view of cost-effectivity and weight-containment - aluminium could better fulfil this purpose.

Figure 2.6: Elements of the periodic table able to make compounds or alloy with alkali metals [34].

2.4 Electrolyte

The electrolyte choice and engineering is critical to assure a proper functioning of the electrochemical cell. It must ensure ionic conductivity, whereas providing a good electronic insulation in order to prevent the current flow inside the cell. The viscosity is another important parameter that affects ion mobility, hence the kinetics of the charge/discharge reactions. Under safety point of view, the thermal stability must be assessed, together with the non-reactivity with the battery components, its toxicity and possibly its environmental friendliness. Moreover, the stability potential window must be coupled to the working voltage of the battery.

Concerning PIB, very little systematic investigation has been performed until now, and many challenges still need to be faced before an industrial deployment of such a technology. As experienced with electrodes, also electrolytes follow the knowledge gained with LIBs and, successively, with SIBs. However, given the high reactivity of potassium metal, severe side reactions are very likely to occur at electrodes interface, damaging the cell or consuming the electrolyte. Poor solubility of potassium salts in common ester electrolytes and possible dissolution of some electrodes in organic solvents are issue to be tackled.

The SEI layer is a critical component, originated by the electrochemical decomposition of the electrolyte on the anode surface. In the first cycles, irreversible reactions occur at the interface, resulting in a barrier which protects both the sides from an excessive degradation and further interaction Figure 2.7. The SEI layer must be able to transfer ions without significantly affecting their mobility, while acting as electronic insulator between electrolyte and electrode [42]. Due

to the massive volume changes given by (de)potassiation, which was considerably smaller in LIBs and SIBs, the mechanical stability of a robust SEI is even more important. Research on its chemistry is still in its early age, being really different from that of LIBs; therefore an accurate engineering of its properties needs to be carried out.
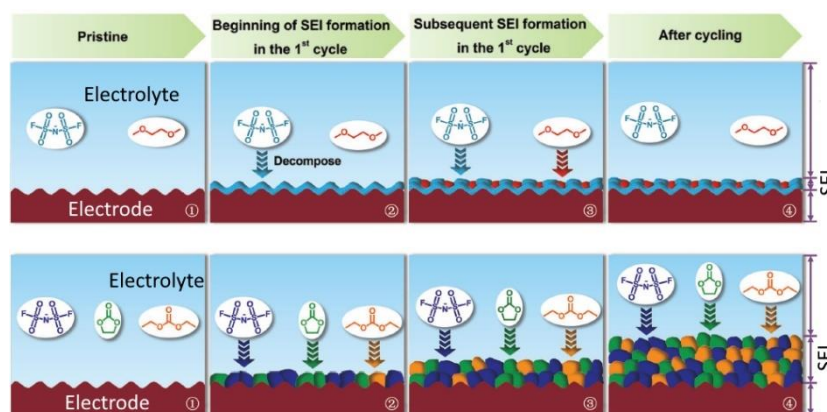
Figure 2.7: Schematic representation of SEI formation in DME (top) and EC:DEC (bottom) electrolyte [42].

2.4.1 Solvent

The solvent is responsible of dissolving the metal salt, requirement met by a high dielectric constant Table 2.1. Besides, the window between melting and evaporation temperature needs to be wide-enough to fit the operating conditions. Organic solvents are the large majority, with ester-based (e.g. EC, DEC, PC, DMC) ones being the most popular. Ester-based solvents provide the weaker solvation structure of K^+ ions (even weaker than Li^+ and Na^+), meaning a faster ion transport assured by the smaller radius of surrounded cation; conversely, the weaker structure given by the smaller de-solvation energy results in enhanced side reactions and a difficulty to obtain concentrated solutions [43]. This is the first suggestion of the challenges posed addressing the problem of a proper electrolyte design. However, EC/DEC is the most investigated mixture because of its large stability window, as well as being a eutectic mixture liquid ad ambient temperature.

On the other hand, ether-based solvents (e.g. DME, DEGDME) have been investigated given the improved solubility of potassium ions, which are surrounded more tightly, resulting in a

stabler system that is less likely to decompose the electrolyte [43]. Moreover, the so-formed SEI layer shows inferior interface resistance and reduced thickness than in ester electrolytes. As shown in (Figure 2.8 a), FSI⁻ possesses a LUMO level lower than DME, therefore its reduction tends to form a homogeneous and inorganic SEI. When coupled with EC/DEC, it appears to be thicker and less stable given its organic-inorganic nature. Instability and more severe side reactions are attributed to the smaller difference between LUMO layers of salt and solvent that may result in simultaneous decomposition [44] [42].
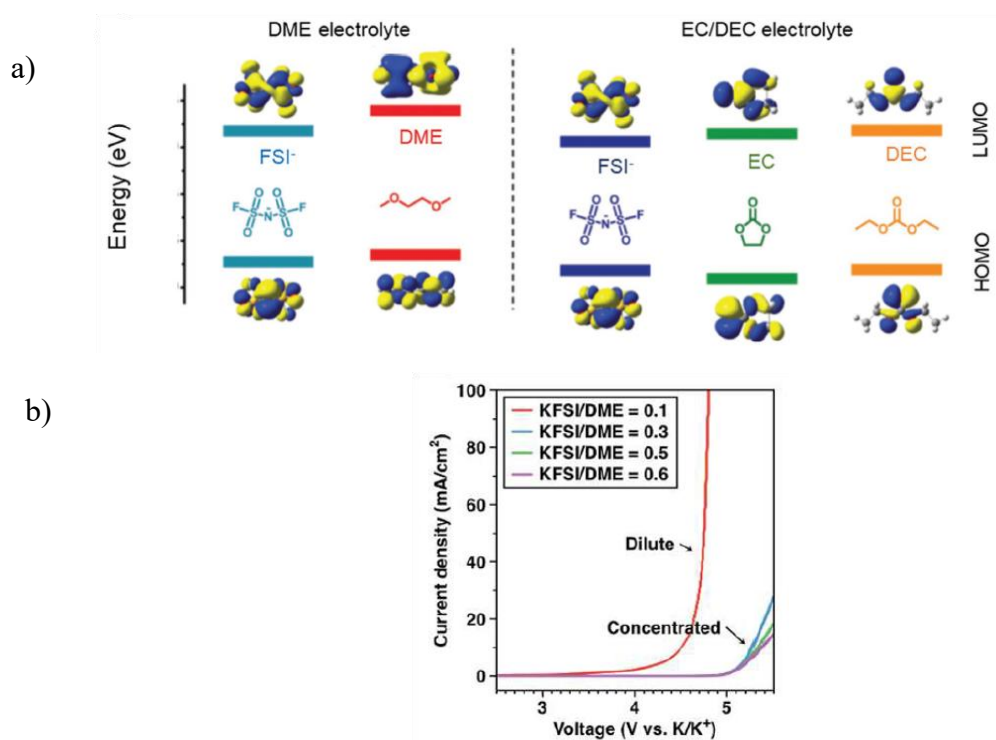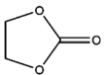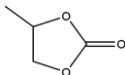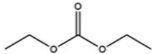
Figure 2.8: a) LUMO and HOMO energy levels of potassium salt anion compared to most employed ether- and ester-based solvents [43]. b) Electrochemical stability of KFSI-DME electrolytes at different molar concentrations [45].

Table 2.1: Properties of the most common solvent, evaluated at 25 °C, unless otherwise specified [46].

Solvent	Structure	Dielectric constant	Viscosity (cP)	Melting temperature (°C)	Boiling temperature (°C)	Density (g cm^{-3})
EC		89.78	1.9 (40 °C)	36.4	248	1.321
PC		64.92	2.53	-48.8	242	1200
DEC		2.805	0.75	-74.3	126	0.969
DME		7.2	0.46	-58	84	0.86
DEGDME		7.3	0.99	-68	162	0.944
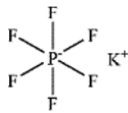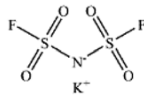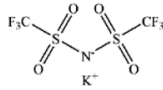
2.4.2 Salt

The other component of an electrolyte is the salt, that is responsible of providing cations and anions from its dissolution. In potassium batteries, the most employed salts are KBF_4, $KClO_4$, KPF_6, KFSI and KTFSI Table 2.2, despite the formers are no longer tested because of their low solubility. KPF_6 is soluble in ester-based solvents, therefore it is herein tested coupled to EC/DEC solvent. It is particularly suitable for electrodes deposited on aluminium due to the passivation effect of PF_6^-, that prevents corrosion, despite the P-F bond can break and form HF [46]. Nonetheless, the observed SEI layer is less stable as previously mentioned and leads to a prolonged low Coulombic efficiency.

Conversely, KFSI and KTFSI (imides) are addressed to form a more stable and thinner SEI layer in ether-based electrolytes, protecting the anode, improving the reversibility of the reaction and with a less relevant impact on its kinetics. It must be noticed that, on an aluminium

current collector, corrosion occurred after repeated cycling at higher potentials [47], issue that was already experienced in LIBs [48]. Finally, in [45] the good passivation effect of KFSI-DME electrolyte is reported, stating that reversible plating and stripping was successfully achieved for more than 200 cycles on a potassium metal anode, whereas failure was induced by both KFSI-EC/DEC and KPF_6-EC/DEC. Furthermore, analysing salt concentration it was possible to conclude that a more concentrated salt allowed a better oxidation resistance of the electrolyte up to a potential of 5 V (*vs*. K^+/K) (Figure 2.8 b), which is an outstanding result that opens research possibilities for high-voltage cathodes.

Table 2.2: Properties of the most common potassium salts [46].

Salt	Structure	Molar weight	Melting temperature (°C)	Aluminum corrosion
KPF$_6$		184.1	575	No
KFSI		219.2	102	Yes
KTFSI		319.2	200	Yes

2.4.3 Additives

It is well-known from LIBs and SIBs that electrolyte additives, such as fluoro-ethylene carbonate (FEC), improve the performances of the cell, therefore their influence on PIBs is now under research. Its addition (2 vol%) in KPF_6-EC/DEC electrolytes was proven to increase the Coulombic efficiency up to 30% during cycling, especially at high voltages [49]. It is stated that the additive was responsible of increasing the active sites of potassium redeposition on the anode, preventing dendrite growth, reducing side reactions and promoting a more even plating.

By contrast, FEC was observed to cause polarization and weakening the SEI layer on a Sn_4P_3@carbon fiber anode [43]. Finally, it is clear that the effect of such an additive cannot be completely resembled to other alkali-metal batteries, hence its employment in PIB electrolytes is still debated.

3 Experimental procedures and methods

In this section, a description of the involved procedures and the instruments employed is proposed, from the electrochemical cell assembly to the characterization of the electrodes and their performances. The experimental part was carried at DISAT laboratories, within the Electrochemistry Group.

3.1 Cell assembly

3.1.1 Electrodes

The electrodes tested were different, but the adopted preparation method was the same and it is here illustrated. It started by the mixing of an active material, a carbon conductive additive,[4] a binder[5] and a solvent in different percentages to prepare a slurry. This method was employed for nanoparticles-based electrodes, namely Prussian blue and titanium dioxide electrodes, while an anodization technique was exploited for the preparation of electrodes based on titanium dioxide nanotubes.

Nanoparticles-based electrodes

First, the raw powders of the active material and the conductive additive (carbon C65) were accurately weighted (Radwag® AS 220C2 balance), crushed in a mortar to disaggregate conglomerates Figure 3.1 and placed into an Eppendorf-tube (2 mL volume) together with two inert zirconia spheres that facilitate the subsequent mixing. By mean of a micro-pipette, the solvent and the binder were added; the first was N-methyl-2-pyrrolidone (NMP), while the second was poly(vinylidene difluoride) (PVDF, 8 wt% in NMP). As last step, the so-obtained slurry was placed in a ball milling machine (Retsch®, MM400) for 15 min at 30 Hz to obtain a homogeneous dispersion.

---

[4] The role of a carbon-based conductive additive is to enhance the electrode conductivity by surrounding the active material, fastening reaction kinetics. Additionally, it absorbs the electrolyte improving the contact with the electrode at the nano-scale [11].
[5] The binder is added to the mixture to improve mechanical stability and adhesion between the electrode components themselves and with the current collector.

To prepare the electrode, a current collector was needed and it was a copper foil for TiO_2 electrodes and an aluminium foil for Prussian blue electrodes. The foil was placed on the automatic film applicator (TQC Sheen®, 133N), which homogeneously spread the slurry with a doctor blade at a speed of 50 mm/s. For each composition, two depositions were done, the thickness of which was manually adjusted to 100 and 200 μm, respectively. The wettability of the current collector foil was enhanced with the help of some solvent droplets. Eventually, the deposition was dried in oven at 55 °C for 1.5 h, fan 30% and aperture 50% to facilitate solvent evaporation. By mean of a highly precise manual cutter, disks of 10 mm and 15 mm (diameter) were obtained and weighted, subtracting the gross mass to determine the amount of active material. The last step before introducing the samples in the glove box was that of drying the disks under vacuum (Büchi®, Glass Oven B-585) for 4 h at 120 °C, in order to remove residual humidity and oxygen.

The obtained electrodes were introduced into a glove box (MBraun®, LABmaster Pro) to assembly the cells in a protected argon-filled environment, constantly monitoring the O_2 and H_2O concentrations, which can hamper the cell due to the high reactivity of potassium metal. Each instrument and material employed in the cell assembly must undergo the thermal treatment under vacuum and must be operated inside the glove box to prevent any oxidizing agent contamination.
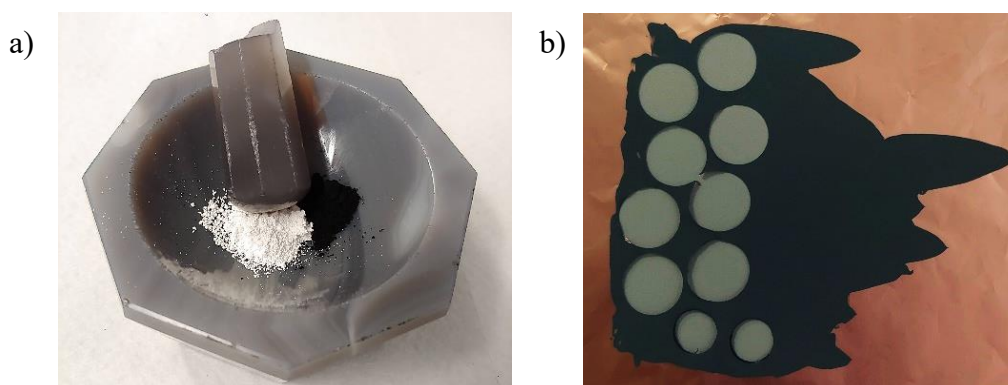
Figure 3.1: a) Agate mortar with titanium dioxide powder (white) and C65 additive (black). b) TiO_2 NPs-based electrode deposited onto a copper foil from which some electrode disks were already cut.

The compositions explored in this Thesis are reported in Table 3.1 and

Table 3.2

Table 3.1: Composition of the anodes.

Ingredient	Commercial product	Supplier	Content
Active material	TiO_2 Hombikat N100	American Elements®	80 wt%
Carbon additive	C65	Imerys®	10 wt%
Binder	PVDF	Sigma Aldrich®	10 wt%

Table 3.2: Composition of the cathodes.

Ingredient	Commercial product	Supplier	Content
Active material	Prussian blue	-	70 wt%
Carbon additive	C65	Imerys®	20 wt%
Binder	PVDF	Sigma Aldrich®	10 wt%

Nanotubes-based electrodes

Self-organized TiO_2 nanotubes arrays were synthesized by controlled anodic oxidation of a titanium substrate, that also acted as a current collector beyond being the supporting layer. To this purpose, a titanium foil was cut and protected on one side by the application of a thin Kapton tape, then it was etched for 1 min in hydrofluoric acid (1 vol% in aqueous solution) to remove the passivating film. The anodic growth took place in two separated steps, the first aimed at providing an ordered template onto which nanotubes were able to successively grow; in the meantime, the sample was ultrasonically cleaned for 1 min to remove disordered nanotubes.

Anodic oxidation was performed in an electrolyte (2.5 wt% distilled water, 0.5 wt% NH_4F, 97% ethylene glycol); applied voltage, time and solution-related parameters (e.g. pH, water content and F^- presence) affect the morphological characteristics of the self-supported nanotube arrays. Also, the temperature is a determining factor, but it is kept constant at 25 °C in our experiments.

The mechanism of formation Figure 3.2 is accurately depicted in [50] and is governed by a competition between anodic oxide formation:

$$Ti + 2H_2O \rightarrow TiO_2 + 4H^+ + 4e^- \tag{3.1}$$
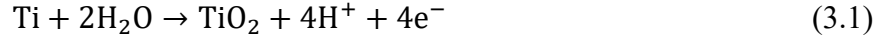
and chemical dissolution of the oxide as soluble fluoride complexes:

$$TiO_2 + 6F^- + 4H^+ \rightarrow [TiF_6]^{2-} + 2H_2O \tag{3.2}$$
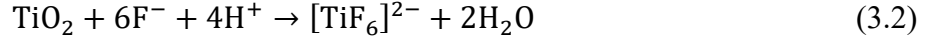
The voltage applied is constant, but the field progressively reduces as the oxide thickness increases, originating a self-limiting process where the steady-state is reached as the oxide dissolution rate equals the oxide growth rate at inner surface, resulting in a progressively reducing titanium foil thickness without thickening the oxide layer. Growth parameter tuning is performed though the applied voltage control, affecting the nanotubes diameter, and anodization time, affecting their length. Some of the samples were also annealed at 450 °C for 30 min in order to crystallize the structure from the amorphous to the anatase phase. A summary of the samples is reported below in Table 3.3.
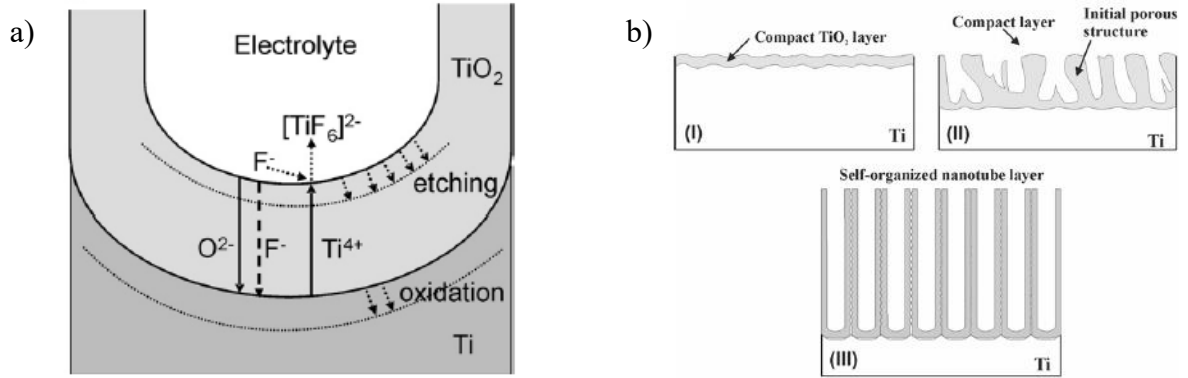
Figure 3.2: a) Schematic representation of anodization in presence of fluoride ions. b) Anodization steps: (I) initial growth, (II) substrate formation with disordered growth, (III) ordered growth after sonic cleaning [50].

Table 3.3: Summary of the samples prepared, with the aim of investigating the impact of both the crystalline phase and the nanotubes length.

Crystalline phase	Anodization time	Tube length	Applied voltage	Tube diameter	Annealing
Amorphous	15 min	6 µm	60 V	80-100 nm	-
	7.5 min	4 µm	60 V	80-100 nm	-
	30 min	10 µm	60 V	80-100 nm	-
Anatase	15 min	6 µm	60 V	80-100 nm	450 °C 30 min

The so-prepared TiO_2 foils were cut in rectangular pieces in order to be employed as electrodes in coin cells prototypes. Differently with respect to what was done for nanoparticles-based electrodes, here the active material is impossible to be weight with a balance, since nanotubes are not simply deposited on the surface (as described above); therefore, the performances will be normalized to the electrode area, measured with a feeler gauge (Mitutoyo®, 547-400S).

3.1.2 Coin cells

This kind of configuration has been employed in cell testing to assess the performances of the investigated materials during galvanostatic cycling. A schematic representation of the coin cell components is reported in Figure 3.3. The configuration effectively employed was the half-cell, which differs from the full cell because one of the electrodes, i.e. the anode, is composed of pure metallic potassium. Here, the cathode is the material to be tested. This configuration is needed to characterize the material without being affected by the anode itself.
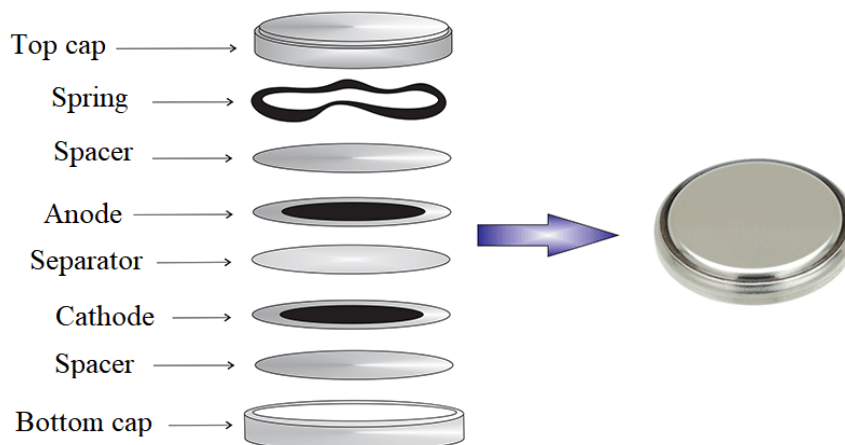
Figure 3.3: Schematic representation of the coin cell components.

The cell was assembled inside the glovebox. The anode was obtained thinning a small piece of potassium, stored in kerosene, and cutting a 16 mm disk with a punching tool. The cathode was weighted before being inserted, in order to estimate the amount of active material. Between the two electrodes, a glass fiber separator (Whatman®, diameter 18 mm) was positioned to prevent short-circuit and it was wetted with the electrolyte solution, i.e. KPF_6 0.8M in EC:DEC 1:1 v:v and KFSI 0.8M in DME. 2 mm-thick metallic spacers were positioned on the back side of the electrodes to improve the contact between them and the top/bottom of the cell. Lastly, the cell was mechanically pressed into a crimper (MTI Corporation®, MSK-160E), sealed applying a pressure of 5 bar, and the starting potential was measured through a digital multimeter in order to verify the absence of short-circuit inside the cell.

3.1.3 T cells

The peculiarity of this cell architecture is the presence of three electrodes Figure 3.4; therefore, it permits more types of measurements. During operations, the potential is measured between the working and the reference electrode, while the current is measured between the reference and the counter electrode. This configuration is generally employed in cyclic voltammetry studies, where a more accurate voltage control is needed; in this work, it has been

employed also to carry out the galvanostatic cycling of nanotubes-based electrodes due to the physical characteristics (i.e., the shape of the samples) of the tested material.

Cell assembly was done inside the glove box-protected atmosphere, weighting a 10 mm-large disk of the electrode and placing it on the top of the stainless-steel cylinder, then inserted in the T-cell and held in position through a nut. On the anode side, pure potassium was employed by cutting a 10 mm-large disk with the punching tool (both for the reference and the counter electrode, except for galvanostatic cycling, for which the reference is not required). Two glass fiber disks were placed between the working and counter electrodes, after being abundantly wetted with the electrolyte solution; the same was done between the reference electrode and the other two. Finally, the potential was measured with a digital multimeter and, if short-circuit was not detected, the cell was manually sealed with Parafilm (Bemis Company®).
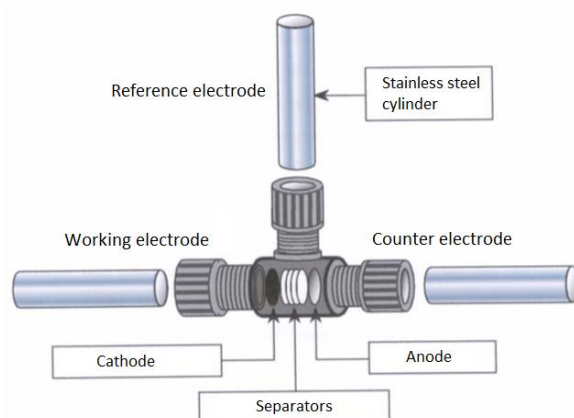
Figure 3.4: Schematic representation of a T cell assembly.

3.2 Electrochemical characterization

These tests are aimed to determine the behaviour of the investigated materials and to estimate the best performances that can be provided by them. Galvanostatic cycling was performed on each electrolyte/electrode combination explored in this Thesis, with the aim of identifying the best ones, that were analysed through cyclic voltammetry, electrochemical impedance spectroscopy and Mott-Schottky's analysis. All the tests were performed at room temperature.

3.2.1 Galvanostatic cycling

In order to perform this test, an Arbin® battery cycler instrument was employed. It imposes a current defined by the user and measures the potential across the electrodes, allowing to perform the cycling charge and discharge of the cell by defining the upper and lower voltage boundaries. During discharge, a negative current is imposed, driving an intercalation/insertion of K^+ in the tested electrode structure, while during charge a positive current is applied, leading a de-intercalation/de-insertion of K^+. The first current applied is always a discharge current because the electrode structure is devoid of charge carriers after cell assembly. The voltage range employed was between 0.01 and 3 V for anodic materials (all the TiO_2 samples) and from 2 to 4 V for cathodic materials (Prussian blue samples).

The current imposed is based on the real amount of active material present in the electrode, subtracting the current collector weight (established as average weight of the foil) to the gross weight, and by multiplying by the fraction of active material in the mixture (3.3),(3.4). Finally, the current is computed by multiplying the active mass to the current density expressed in $A\,g^{-1}$. When the active mass was not measurable, i.e. in nanotubes-based electrodes, it was scaled out to the active area, imposing a current density expressed in $mA\,cm^{-2}$.

$$m_{att} = f_{att} * \left(m_{gross} - m_{cc_{foil}}\right) \tag{3.3}$$

$$I = I_{density} * m_{att} \tag{3.4}$$

The standard program employed in cell testing is reported in Table 3.4.

Table 3.4: Current densities imposed during normal 200 cycles. *: [mA cm^{-2}] in nanotubes-based electrodes. **: comparison with initial cycles for capacity retention. ***: final series to observe cell stability.

Current density $(A\ g^{-1})^{*}$	Number of cycles
0.05	10
0.1	10
0.2	10
0.4	10
0.8	10
1.0	10
2.5	10
5.0	10
0.05**	10
0.1***	110

Results gathered from this test are generally plotted in a specific capacity (3.5) (3.7) and Coulombic efficiency (CE) (3.6) *vs.* cycle number graph.

$$c_D = \frac{C_D}{m_{att}} \tag{3.5}$$

$$CE = \frac{C_D}{C_C} * 100 \tag{3.6}$$

Another helpful plot is the voltage *vs.* specific capacity for charge and discharge curves, which is aimed to highlight the occurrence and the reversibility of reactions. The shape of these curves allows to recognise residual polarization upon cycling, that hampers the reversibility of charges (de-)insertion, suggesting structural and chemical alterations resulting in poor cell cyclability. Generally, a voltage plateau or a quasi-linear region in charge/discharge curves is advisable because it identifies the best operating window of the cell. Before and after this region, the

voltage rapidly drops and drives side reactions that may be irreversible, affecting the cycling stability and long-term performances.
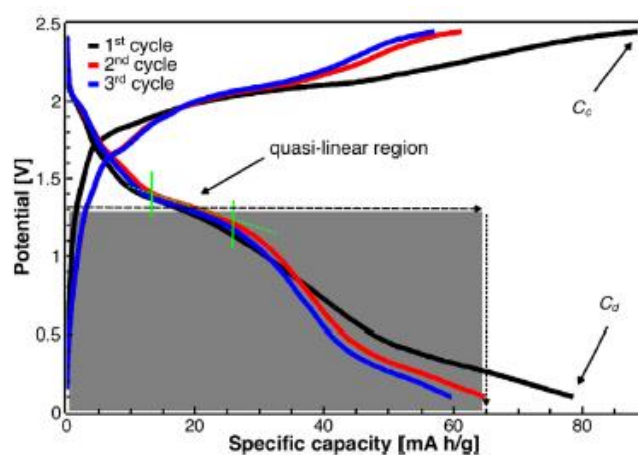
Figure 3.5: Charge/discharge curves during subsequent cycles [20].

3.2.2 Galvanostatic long cycling

As regards the best cells, prolonged galvanostatic tests were performed with the Arbin® battery cycler to assess both the cycling stability and the lifetime. Two tests were carried out for each experimental condition, but with the same electrode/electrolyte composition, both repeated until failure of the cell

Table 3.5: Long cycling test. After the 160th cycle, it starts again with the first current density value. *: [mA cm^{-2}] for nanotubes-based electrodes.

Current density $(A\ g^{-1})^*$	Number of cycles	Repetition
0.05	20	
0.1	20	
0.2	20	
0.4	20	
0.8	20	Until failure
1.0	20	
2.5	20	
5.0	20	

Table 3.6: Long cycling test. Usually, this test takes months and involves temperature control to simulate real operating conditions; anyway, this test represents a preliminary study of our electrochemical system. *: [mA cm^{-2}] for nanotubes-based electrodes.

Current density $(A\ g^{-1})^*$	Number of cycles	Repetition
0.1	-	Until failure

3.2.3 Cyclic voltammetry

This test is performed with a VSP-3e Potentiostat (BioLogic®, 4 channels), where a voltage is applied and the response current of the cell is measured. A T cell configuration with three electrodes is here needed. Results are then reported in a voltage-current voltammogram, which allows the identification of reactions occurring inside the cell through current peaks

(Figure 3.6 a). Additionally, it provides an indication on the reversibility of the reactions, the stability of intercalation/deintercalation of K^+ ions and the kinetics of the process. The system is ruled by the Nernst's equation, that predicts how the system will evolve upon a change of the applied potential or of the concentration of species in solution (3.7), where E^0 is the standard potential of a species, F is Faraday's constant, R is the universal gas constant, n is the number of electrons, T is the temperature, [Ox] and [Red] are the concentration of species.

$$E = E^0 + \frac{RT}{nF} \ln \frac{[Ox]}{[Red]} \tag{3.7}$$

The potential of the working electrode is linearly varied in a voltage window through the definition of a scan rate (voltage variation per unit of time) and measured with respect to the reference electrode. In this work, the reference electrode is potassium, therefore - in the voltammogram - results will be plot with respect to K^+/K. The scan rate is a critical parameter because it controls the kinetic of the reaction taking place, since it leads the electron transfer between the molecular orbitals of chemical species. A faster scan rate reduces the diffusion layer size, increasing the peak current [51]; conversely, it decreases the resolution of the voltammogram because the merge of two close peaks may occur. To properly select a scan rate, a comparison has been performed, the results of which are reported in (Figure 3.6 b): using the slowest scan rate, the resultant curve is more detailed, therefore 0.1 mV s^{-1} will be the employed for successive tests.
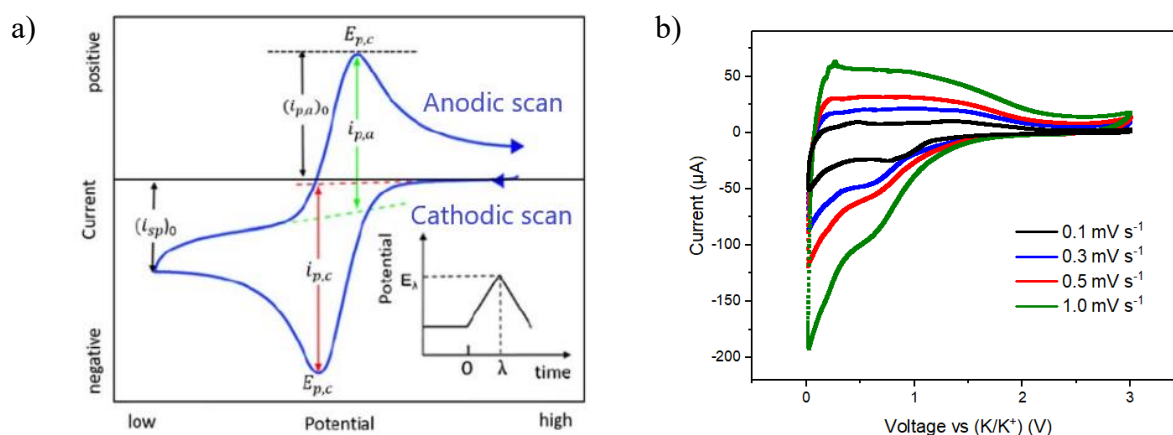
Figure 3.6: a) Typical duck-shaped CV plot. b) Effect of the scan rate on TiO_2 NPs/KFSI 0.8 M in DME. Using a faster scan rate (green), peaks are more pronounced, but tend to be merged with respect to a slower one (black).

Table 3.7: Parameters adopted for the CV test.

Material	Lower voltage limit	Upper voltage limit	Scan rate	Cycles
Anodic	0.01 V	3.0 V	0.01 mV s^{-1}	3
Cathodic	2.0 V	4.0 V	0.01 mV s^{-1}	3

3.2.4 Electrochemical impedance spectroscopy (EIS)

EIS is an AC technique that consists in applying as input a potential (E_{app}), on the top of which a small sinusoidal modulation is imposed (3.8) (usually not exceeding 10 mV) over a wide range of frequencies (10 mHz – 100 kHz), while measuring as output a sinusoidal current response (3.9). Due to the superficial resistive or capacitive behaviour, the response will be shifted by a phase angle that allows to evaluate each contribution [52]. Differently, the CV is a DC technique that does not allow the differentiation of those component. The evaluation then proceeds computing the impedance as the ratio between the potential and the current (3.10). The results are then plotted in a Nyquist's diagram (Figure 3.7 a) (imaginary over real part of

the impedance) or in a Bode's diagram (Figure 3.7 b) (phase angle or impedance module over frequency).

$$E(t) = E_{app} + E_0 * \sin(\omega t) \tag{3.8}$$

$$I(t) = I_0 * \sin(\omega t + \varphi) \tag{3.9}$$

$$Z(\omega) = \frac{E(t)}{I(t)} \tag{3.10}$$
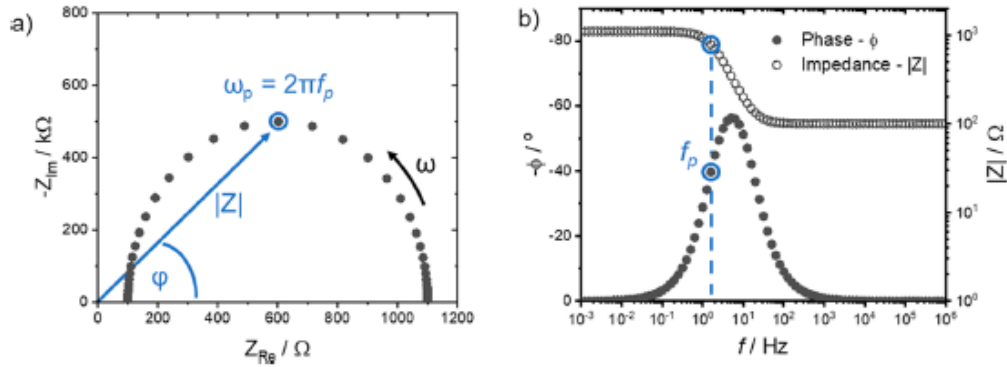
Figure 3.7: a) Nyquist's plot, each point is taken at a different frequency, the latter increasing from the right to the left. b) Bode's plots, again each point is taken at a different frequency, but the dependence is clearer [52].

The interpretation of EIS data is a major challenge because it requires the identification of a suitable electrical circuit model able to fit them properly. The next step is to relate each component of the fitting circuit to a physically occurring phenomena to understand their contribution to the surface impedance. Furthermore, the difficulty of this approach lies in the identification of the correct model, since the experimental results fitting is not unique, and using a wrong model inevitably leads to the wrong conclusions. The software employed to model the equivalent electric circuit is ZView 3.2®. The main components employed in the circuit model are reported below:

Resistor $Z = R$

It describes Faradaic electron transfer across surface layers of different elements, such as the electrode, the SEI layer and the electrolyte. The determination of each contribution is usually difficult, therefore two main resistances can be found in an equivalent circuit: the system equivalent resistance (R_0), equal to the intersection with the x axis in the high frequency region, and the charge transfer resistance (R_{ct}), equal to the point where the semicircle crosses the x axis at medium frequencies. The latter is a model of the resistance encountered by electrons in the electrode/electrolyte transfer. They are usually series-represented in order to account for any resistance met during transfer.

Capacitor $Z = \frac{1}{j\omega C}$

It accounts for complex phenomena of charge accumulation at the solid/liquid interface, the major contribution of which is the electric double layer. Due to the electrically charged electrode surface, opposite charges in the liquid phase are disposed in such a way that try to balance the electrostatic force, leading to a more difficult charge motion. No chemical reactions are involved here and the charges are transferred by diffusion only.

Constant phase element $Z = \frac{1}{Q*(j\omega)^\beta}$

It represents a capacitor that keeps constant the phase and provides the best fitting of the characteristic semicircle. It is suitable to model real double layer and charge accumulation, rather than a pure capacitor, because it accounts for non-ideality on the surface, such as roughness and irregularities. In the equivalent circuits, it is generally represented in parallel to the charge transfer resistance in order to model the two contributions to the total current, sum of both Faradaic and non-Faradaic. In the equation describing its impedance, the β exponent ranges between 0 and 1; when it is equal to 1, the behaviour is ideal and Q becomes the capacitance C.

Warburg's element $Z = \frac{\sigma\sqrt{2}}{(j\omega)^\beta}$

It describes the diffusion of mobile charges in the low-frequency regime, ruled by mass transfer and diffusion coefficient of charge carriers σ. In the Nyquist's plot, it is usually detected by a linear dependency with the frequency with a slope of 45° and a β coefficient of 0.5. If the

measured data show a larger slope, other capacitance effects are relevant and a constant phase element can better approximate the experimental results. In the equivalent circuit, a series inclusion could be reasonable since its contribution is added in a frequency regime different than the elements previously described.

The EIS measurements were not performed alone, but they were carried out with CV in order to have a multiple and complementary approach to the cell study. Some open-circuit voltage (OCV) detection steps, i.e. a static measurement of the cell voltage for 5 min, have been added in order to assess cell state and stability. A VSP-3e Potentiostat (BioLogic®, 4 channels) was used, using the EC-Lab® software to process data.

3.2.5 Mott-Schottky's analysis

When semiconductors (e.g. TiO_2) are employed as electrodes, being in contact with an electrolyte and applying a potential, the space charge redistribution in the latter (electric double layer) affects the space charge distribution in the semiconductor at a larger distance. This is because the concentration of conductive species (holes or electrons) is much smaller in the semiconductor. Due to this effect, potential bending appears on the surface: for n-type - semiconductors, electrons tend to migrate to the solution, causing an upward bending associated to the induced positive space charge region. At a certain distance, this effect is no longer observed and the potential is called "flat-band potential". Its value, as well as the donor density, can be electrochemically determined and it is important to characterize the electrode/electrolyte interaction [53]. The depletion region capacitance is reported to follow the Mott-Schottky's equation (3.11), where C_{sc} is the semiconductor electrode specific capacitance (F cm^{-2}), ε_r is the dielectric constant of the semiconductor (-), ε_0 is the dielectric permittivity of vacuum (8.85 x 10^{-14} F cm^{-1}), e is the electron charge (1.602 x 10^{19} C), E_{fb} is the flat-band potential [V], k_B is the Boltzmann's constant (1.38 x 10^{-23} J K^{-1}), T is the absolute temperature (K) and N_D is the concentration of donors (cm^{-3}).

$$\frac{1}{C_{sc}^2} = \frac{2}{\varepsilon_r \varepsilon_0 e N_D}\left(E_{app} - E_{fb} - \frac{k_B T}{e}\right) \tag{3.11}$$

The properties of the sample can be obtained by plotting and analysing the specific capacitance per unit area over the potential Figure 3.8. Mott-Schottky's equation was derived for the metal/semiconductor interface, but still holds true for the metal-electrolyte interface [54]. It predicts a linear relationship when a semiconductor band bending in the depletion layer is present, therefore the equation can be used in the highlighted portion of the curves shown in Figure 3.8. The flat-band potential is determined from the intercept with the x-axis, whereas the donor concentration can be obtained by applying (2.2), where the slope of the Mott-Schottky's curve is present at the denominator. A positive slope of the linear part describes n-type semiconductors, as is the case for TiO_2.

$$N_D = \frac{2}{\varepsilon_0 \varepsilon_r e \frac{d\left(\frac{1}{C_{sc}^2}\right)}{dU}}$$

(3.12)
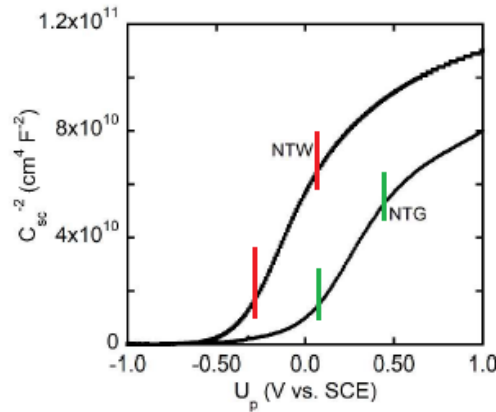
Figure 3.8: Mott-Schottky's plots obtained for anodically-grown TiO_2 nanotubes in two different electrolytes [55]. The semiconductor behaviour is highlighted in the linear portion of the curves.

A technique called staircase potentiostatic EIS (SPEIS) is therefore employed in the BioLogic® potentiostat to drive this test. It consists of an EIS measurement (100 kHz – 10 mHz)repeated

at every potential in the selected window (0.01 – 3 V, 0.1 V step^{-1}). Hence, results are processed with the EC-Lab® software.

3.3 Structural and morphological characterizations

Beyond the electrochemical characterizations, it is useful to analyse the morphology and the crystallinity of a sample, in order to identify any possible variation in the sample structure, aimed to identify the occurrence of degradation or transformation processes that can contribute to the electrode performances. These structural and topographical alterations can hamper or enhance the intercalation mechanism of K$^+$ ions.

Tests have been carried on pristine, cycled and half-cycled electrodes, in order to detect any difference between the fresh material, the cycled material with K$^+$ ions inserted and the cycled material with K$^+$ ions de-inserted.

3.3.1 XRD analysis

This is a non-destructive technique; hence, it is generally performed before any other post-mortem analysis. It has been employed in this work to detect the crystallographic structure and atomic arrangement of the sample. An X-ray beam, generated by a Cu Kα source (λ = 1.5406 Å), is sent to the target and diffracted following the Bragg's law (3.13), carrying information on the crystal plane distance d through the diffraction angle θ. The resulting chart is produced by constructive interference at specific wavelengths [56], which produces characteristic peaks corresponding to the crystalline phase. Hence, it is compared with reference patterns in the PANalytical X'Pert® software to identify a possible match. The instrument employed is an X'Pert® Powder DY 3539. In order to prepare the sample, electrodes were scratched from the current collector, and the active material was powdered.

$$2d \sin\theta = n\lambda \qquad (3.13)$$

3.3.2 Field Emission-Scanning Electron Microscopy (FE-SEM)

This is an ex situ surface microscopy that employs electrons instead of light to generate a detailed image of the sample, due to the smaller wavelength of the first and, therefore, with higher resolution. A strong potential difference is responsible for the electron beam generation, which is more focused and brilliant than a normal filament (SEM) microscopy. The sample surface is scanned through the accelerated electron beam, the inelastic interaction of which generates secondary electrons [57]. The angle and the energy of emitted electrons carry information of the target surface. An Everhart-Thornley detector is responsible of collecting them, translating into a high-resolution image. In the electron column, vacuum is created to minimize gas molecules presence and prevent scanning alterations. For this characterization, a ZEISS® Supra 40 microscope was used.

Samples were prepared cutting top and cross sections of electrodes and attached to specific supports by mean of a conducting tape, which prevents incident electrons to be reflected, corrupting the image. High-energy incident electrons alter and ruin the sample, making this a destructive test to be performed generally after the XRD analysis.

3.3.3 EDX analysis

Energy-dispersive X-ray analysis provides a surface mapping of elements estimating their content proportion. X-ray generated by electron beam collision in the FESEM instrument are detected by a secondary receiver. The energy carried by the X-ray is characteristic of each element; heavy elements are generally easier to detect than lighter ones and with greater accuracy [58].

4 Results and discussion

In this section, the results obtained in the electrochemical and morphological tests are reported. Briefly, Table 4.1 shows a summary of the investigated samples. The active materials were systematically studied in order to understand the impact of the electrolyte and of the material deposition, as well as its crystalline structure, in order to perform a multi-directional comparison. First-step test, i.e. galvanostatic cycling, was carried for all the samples listed, while second-step analyses, i.e. cyclic voltammetry, Mott-Schottky's analysis and EIS analysis, were carried only with the configurations that showed the best response.

Table 4.1: Summary of the cell configurations that were tested. The electrolytes employed are KFSI 0.8 M in DME and KPF_6 0.8 M in EC:DEC.

Nanoparticles-based (NPs)			*Nanotubes-based (NTs)*		
Active material	**Thickness**	**Electrolyte**	**Active material**	**Growth time**	**Electrolyte**
TiO₂, anatase	200 μm	KFSI	**TiO₂, amorphous**	15 min	KFSI
		KPF_6			KPF_6
	100 μm	KFSI		7.5 min	KFSI
		KPF_6			KPF_6
PB	200 μm	KFSI		30 min	KFSI
		KPF_6			KPF_6
	100 μm	KFSI	**TiO₂, anatase**	15 min	KFSI
		KPF_6			KPF_6

4.1 TiO₂ nanoparticles

The first analysis carried out on titania nanoparticles was aimed at identifying the impact of slurry deposition thickness and electrolyte on the cell performances. A summary of the results is reported in Figure 4.1, where the specific capacity (a) and Coulombic efficiency (b) are plotted *vs*. cycle number. The 100 µm-thick sample delivered a larger specific capacity with both the electrolytes. It was attributed to a better exploitation of the active material area, assuming that, with a thicker deposition, the electrolyte was not able to wet the deeper portions of the electrode. It can be also noticed that, regardless the thickness, cells that employed KFSI-based electrolyte were more performant, showing a more stable behaviour, than the ones employing KPF_6 electrolyte. This behaviour is common for ether-based electrolytes, which are reported to create a stable and thinner SEI layer [45], that prevent further reactions. Conversely, carbonate-based electrolytes present ongoing side reactions that may lead to a growing SEI layer. It progressively thickens and covers the porous structure, eventually reducing the capability to accommodate ions [59]. The low CE shown by the blue curve in Figure 4.1 may be determined by these proceeding reactions.

100 µm-thick cell in KFSI demonstrated good capacity retention of 82.1% (cycle 10th *vs*. cycle 100th), which increased to 87.4% at cycle 200th, also showing some sort of capacity activation. The Coulombic efficiency was, however, above 98%, proving the good reversibility of the insertion mechanism. By contrast, the reversibility in KPF_6 electrolyte was generally poorer, indeed a rapid capacity fading was observed, especially with thinner electrode layers.
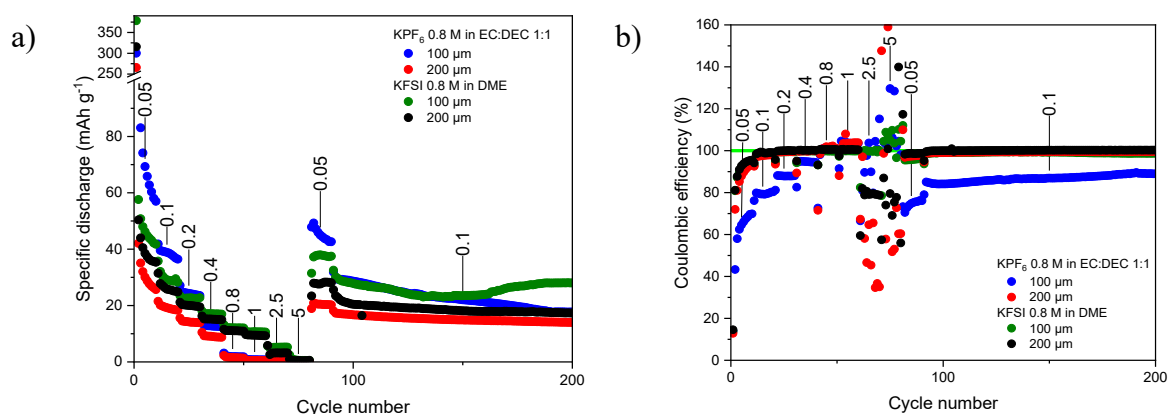
Figure 4.1: Comparison of TiO₂ NPs electrodes at different current densities (A g⁻¹) with respect to thickness and electrolyte. Specific discharge (a) or CE (b) *vs*. cycle number.

In Figure 4.2, the charge/discharge curves are reported at different current rates, ranging from 0.05 to 5 A/g, and at different cycles for TiO$_2$ NPs 100 µm in KFSI. The rate capability shown is relatively poor, because the capacity halves when the current is increased from 0.1 A g^{-1} to 1 A g^{-1}, highlighting the slow insertion mechanism of large-sized K$^+$ ions into the active sites. At higher current ranges, the intercalation does not have enough time to be completed. The electron charge accumulation is, hence, not screened by potassium ions insertion, and the voltage of the cell suddenly rises, originating the steeper profiles of the curves at higher current rates. This can be induced by longer diffusion pathways for cations into the electrode, that are not physically able to reach the hosting sites. Thus, reducing these channels length could significantly improve the rate capability of the cell [60]. At the same time some cations may remain trapped, blocking the site and causing polarization of the battery, which decreases the potential window and consequently the storable energy. Despite the low rate-capability, TiO$_2$ NPs show very good reversibility after 100 and 200 cycles, where initial curve (cycle 15th) could be almost completely overlapped. It suggests that the nanoparticulate anatase structure is not damaged upon cycling and repeated (de-)insertions [61, 62]. On the other hand, the polarization shown by the curves is relevant and no discharge plateau can be recognised.
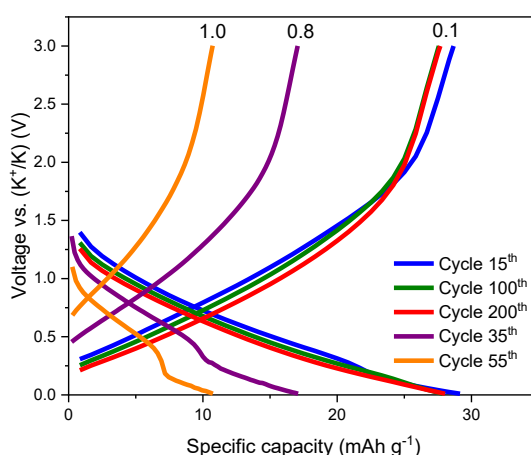
Figure 4.2: Charge/discharge curves of TiO$_2$ NPs 100 µm in KFSI at different current densities (A g^{-1}).

4.1.1 Morphological analysis

TiO$_2$ NPs 100 µm in KFSI/DME were investigated through the XRD technique in order to detect any change in the crystalline structure before and after full cycling. A different crystalline rearrangement is also possible between the potassiated and de-potassiated electrode, therefore also these two different configurations were screened. A potassiated electrode is obtained if the last cycle employed is a discharge one, whereas a de-potassiated is obtained if it is a full charge. The XRD patterns reported in Figure 4.3 shows a purely anatase composition of the pristine electrode as declared by the supplier. After cycling, the ex-situ analysis of both the potassiated and the de-potassiated samples still present the evident peaks attributed to the anatase phase. Some other smaller peaks became visible after cycling, but they were associated to electrolyte and salt degradation at lower voltages [61]. Finally, no significant crystalline phase change was detected through this technique, other than some disordering of the structure suggested by the slightly broader diffraction peaks of the anatase phase [62].
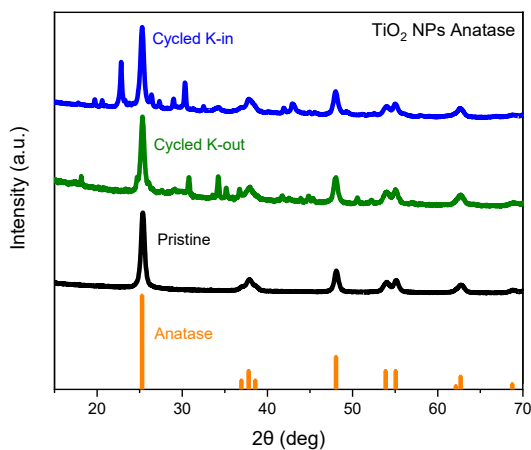
Figure 4.3: XRD patterns for the TiO$_2$ NPs samples pristine and cycled. The reference pattern for the anatase crystalline phase is also plotted.

FE-SEM images were captured in order to visually compare the morphology of the pristine and cycled electrode. Figure 4.4 a-c shows the fresh electrode, suggesting that a thickness of roughly 14 µm is obtained from drying a slurry deposition of 100 µm. It can also be observed that the porous structure tends to aggregate in conglomerates made up by particles, the size of which is around 50 nm. From the cycled electrode (Figure 4.4 d, e), no evident morphological

changes were detected. Particles size was still in the nano-size range and the mechanical cohesion of the electrode was verified since its thickness remained almost unchanged. In the last figure some planes connecting particle conglomerates are evident, which might be attributed to electrolyte degradation, side reaction products or salt depositions.
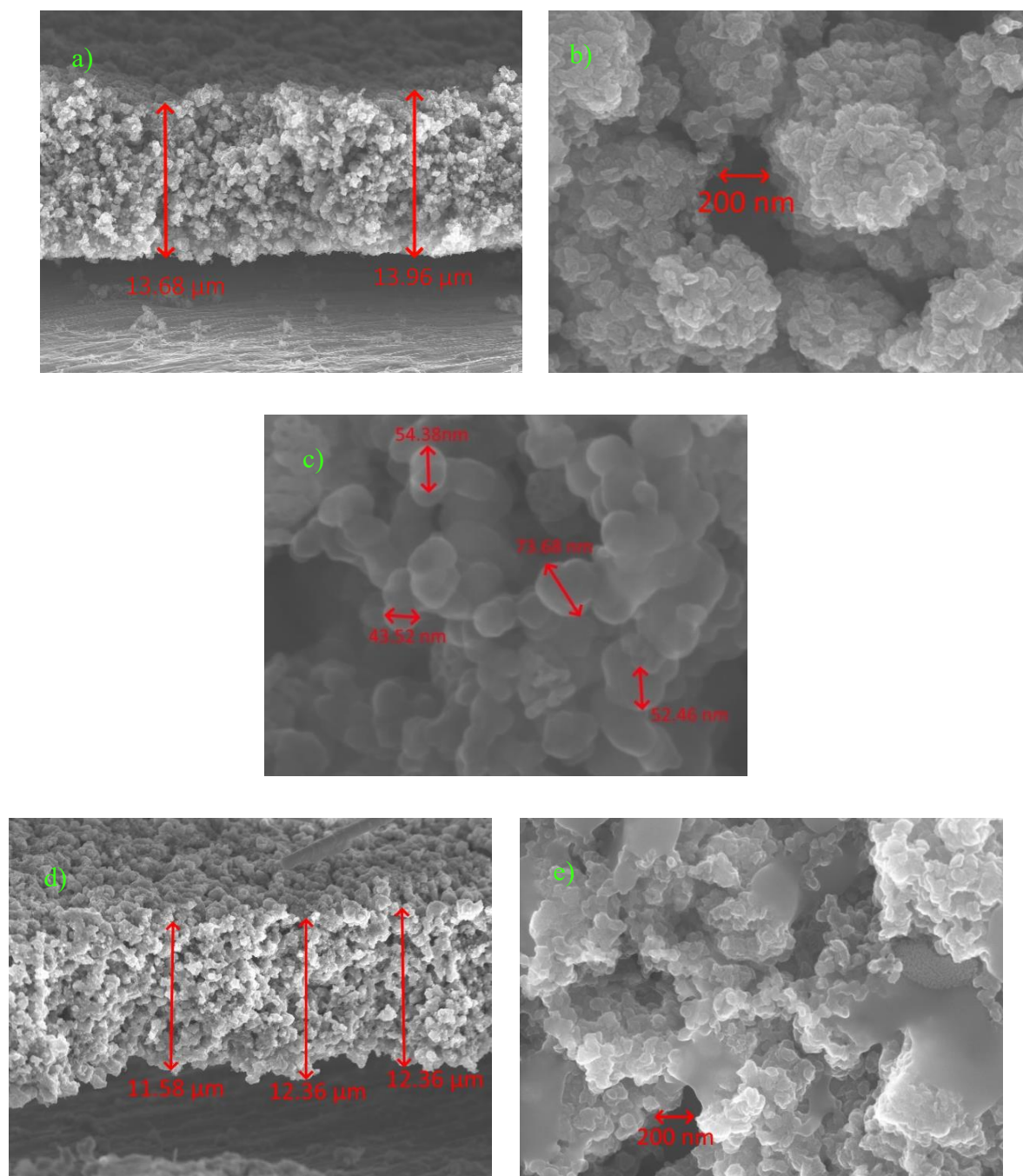
Figure 4.4: FE-SEM images of the TiO_2 NPs pristine (a, b, c) and cycled (d, e) electrode. a, d are in cross section, whereas (b, c, e) are in top view.

4.1.2 Cyclic voltammetry

This test helpfully contributes to the identification of reactions occurring inside the cell and the voltage at which they take place. The CV was performed on the fresh cell and the voltammogram is reported in (Figure 4.5 a). A massive change between the first and second cycle is clearly evident, with a narrow cathodic peak at around 0.8 V associated to the formation of the SEI layer and the decomposition of the electrolyte [59]. From the stability window of salt and electrolyte, being the LUMO level of KFSI lower than that of DME, the decomposition is more likely to be attributed to the former [63]. Given the significant change between the first and the second CV cycle, the huge difference between the specific capacity of the first and second cycle shown by NPs in Figure 4.1 can be understood. It provides an indication also of the quality of this electrolyte, that remains stable after an initial decomposition, preventing further reactions and continuous degradation.

The redox couple Ti^{3+}/Ti^{4+} was associated to the peaks at 1.46 V (de-insertion) and 0.83 V (insertion), and centered at around 1.2 V, which is coherent with the linear region in the charge/discharge curves of the material Figure 4.2. It can also be noticed a relatively stable behaviour after the first cycle, despite a slight reduction of the peak current on the anodic branch. The voltammetry was then repeated after 100 cycles in order to observe the evolution of this de-insertion peak (Figure 4.5 b) and in order to verify whether a contribution of the carbonaceous additive could be deduced. Indeed, after 100 cycles the anodic peak disappeared, suggesting an irreversible degradation on the capability of TiO_2 of releasing K^+ ions. Conductive carbons usually show cation uptake at low voltages [59, 62], which contributes to the specific capacity of the cell and might justify the larger voltammogram shape in this region. Such an analysis is proposed in Annex I, verifying that the impact is not negligible at all.
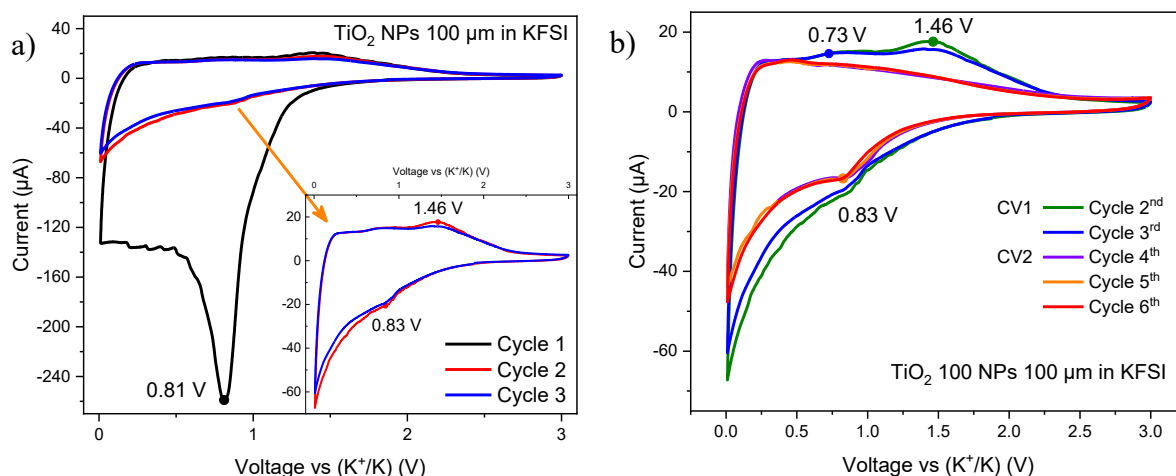
Figure 4.5: Voltammogram of TiO$_2$ NPs in KFSI: a) first three cycles of CV with inset excluding the first one; b) comparison with last three cycles of CV after 100 GC cycles.

4.1.3 Electrochemical impedance spectroscopy

This technique is employed to evaluate the evolution of the resistive and capacitive phenomena occurring though all the cell layers (interface impedance between electrode and electrolyte) at different frequencies between 100 kHz and 10 mHz. On this purpose, a first EIS measurement was performed on the fresh cell, then a second one was performed after three CV cycles, which are assumed to create a stable SEI layer. This assumption comes from the stability reached by the cell and observed after the first cycle of voltammetry, since former irreversibilities are no longer present. The comparison between the results of the two EIS allows a first estimation of the so-formed SEI layer behaviour in terms of impedance. An equivalent circuit is then used to quantitatively analyse the Nyquist's plot in order to understand the contribution of different phenomena involved in the charge transport across the surfaces. The physical relevance of the fitting data is the most challenging topic due to the difficulty of interpretation and the multiple possible equivalent circuits that may provide a good approximation.

Basing on the Nyquist's plot of TiO$_2$ NPs presented in (Figure 4.6 a), the equivalent circuit reported in (Figure 4.6 b) was used to model the data, proposing a variation of the Randles' circuit [52]. R$_1$ is the series resistance that accounts for the system resistance, related to the electrolyte, separator and electrodes. R$_2$ and CPE$_1$ are representative of the electrode surface, modelling the charge transfer resistance (Faradaic) and the double-layer capacitance (non-

Faradaic, respectively. These components are inserted in parallel because of their double contribution and since at their endpoints the same voltage is applied. A CPE is used rather than a pure capacitor because it fits better the roughness of such a nanoparticulate electrode where the surface is not smooth. The number of semicircles shown in the Nyquist's plot affects the number of couples R-CPE, employing the general rule of one per semicircle. In the fresh cell, the SEI layer was not formed yet, therefore only one semicircle is shown. However, given the morphological nature of the NPs electrode, a SEI layer is thought to be created surrounding almost each nanoparticle [59]. Hence, SEI resistive and capacitive contribution is very likely to appear merged to the charge transfer semicircle related to the electrode/electrolyte interface, given their similar time constant [64]. Indeed, the cycled cell shows only one evident semicircle. Finally, CPE_2 could be representative of the charge diffusion across the metal oxide surface at lower frequencies. Due to the slope larger than 45° of the final stretch shown by the first cycle, it was preferred over a Warburg's element. From Table 4.2, where the results of fitting are listed, a slight increase on the system resistance R_1 can be seen, remarking the electrolyte stability. Conversely, the charge transfer resistance shows an impressing increase, which denotes a slowdown of the reaction kinetics. This increase is witnessed also by the significant growth in the semicircle diameter, in agreement with the capacity fade observed after the first discharge during cycling Figure 4.1 [31].
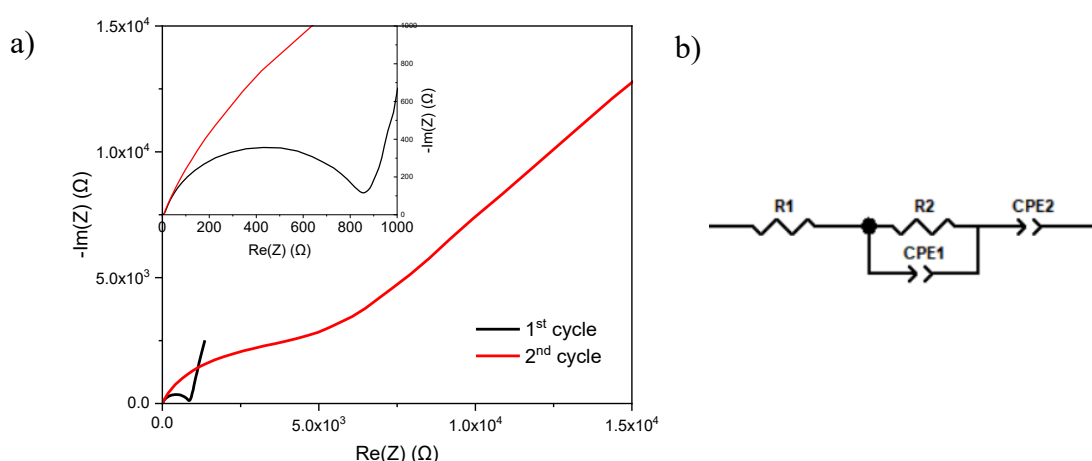
Figure 4.6: a) EIS results of TiO_2 NPs of the fresh cell and after the CV, the inset reports a narrower impedance window in the high frequency region. b) Equivalent circuit used as model to fit the data.

Table 4.2: Results of the fitting of TiO_2 NPs based on the equivalent circuit.

		R_1	R_2
Fresh	Value (Ω)	4.31	863.9
	Error (%)	-	0.41
After CV	Value (Ω)	6.26	3501
	Error (%)	-	2.08

4.1.4 Mott-Schottky's analysis

This analysis was carried on the TiO_2 anatase nanoparticles sample. Since the donor density varies with the tested frequency, the semiconductor properties were evaluated at a specific one (the choice of frequency is reported in Annex II). The intercept of the tangent to this curve, as shown in Figure 4.7, was used to obtain the flat-band potential and its slope to compute the donor density through the equation (3.12), assuming a dielectric constant equal to 120 [65].The upward-shaped curve is consistent with the n-type semiconductor properties of TiO_2, attributed to the Ti^{4+} interstitial ions and oxygen vacancies inside the lattice that contribute to an excess of electrons [66]. The results are reported in Table 4.3, but further considerations follow the same analysis performed on the nanotubes-based samples.
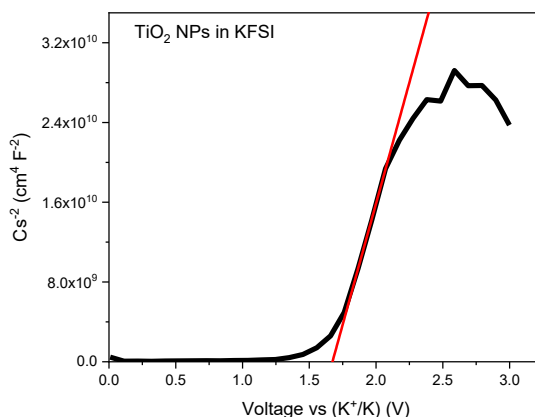
Figure 4.7: Mott-Schottky's plots for TiO_2 anatase NPs. The slope of the linear portion is 4.86 $\times 10^{10}$ cm^4 F^{-2} V^{-1}.

.

Table 4.3: Results of the Mott-Schottky's analysis for TiO_2 nanoparticles.

	Flat-band potential	Donor density (cm^{-3})
TiO$_2$ nanoparticles	1.55 V	3.83 x 10^{19}

4.2 TiO$_2$ nanotubes

TiO_2 anatase nanotubes were addressed in the study as counterpart of anatase nanoparticles. Initially, they are compared to the correspondent amorphous nanotubes, in order to evaluate the impact of the crystalline phase on the cell capacity without considering the nanostructure. The exploratory study then proceeded in the evaluation of the effect of nanotubes length, consequent to the different anodization time, eventually leading to a comparison with the nanoparticles as last step.

The effect of the nanotubes crystallization on their ability to accommodate K^+ ions is evaluated by comparing two different sets of samples, the anodization time of which was 15 min. Half of the samples underwent an annealing process aimed at crystallizing their structure into anatase. The results of the galvanostatic cycling are reported in Figure 4.8, where the two different electrolytes employed are also highlighted. It is noteworthy that amorphous NTs are

characterized by higher specific capacities than their crystalline counterpart. In [67], it was firstly ascribed to the higher presence of defects, voids and a more generally disordered structure, able to accommodate K^+ ions. Despite being reported for sodium insertion, a more difficult uptake in the more rigid crystalline structure could be reasonably derived for larger-size K^+ ions, given the evident differences in the delivered capacity among samples. In (Figure 4.8 b, d), it is clearly depicted the low CE in the first few cycles at low current density. Several mechanisms are addressed to cause this initially low CE, which still needs further investigation. Generally, they are classified in: initial irreversible electrolyte decomposition, side reactions and poor reversibility of the potassiation/depotassiation reaction [68]. The latter could be addressed as the reason behind the irreversibility in the amorphous phase. Defects increase the active sites, but may also act as a trap for the cations that may remain stuck after initial insertion. In KPF_6/EC:DEC electrolyte, the initial capacity loss is even more pronounced than in KFSI/DME. Employing FSI^--rich salt, the initial decomposition at low current ranges is more favourable, forming a thinner and more robust SEI layer, which suddenly prevents further side reactions [69].

It should also be noticed that TiO_2 amorphous NTs in KFSI/DME show some sort of initial capacity activation at low current densities, that may come from a structural rearrangement upon cycling in the first K^+ insertions/deinsertions, which activates new sites and channels [67], [70]. Amorphous NTs are also characterized by an outstanding cycling stability with capacity retention of 93.9% after 100 cycles and 86.4% after 200 cycles, with CE above 97.8%. In some works, it has been attributed to the disordered phase, able to accommodate stress relaxation during large ions insertion/deinsertion and reduce permanent channels deformation that could hamper successive ion hosting [33].

After the determination of the most appropriate crystalline structure, which emerged to be the amorphous one, the focus moved towards the identification of the most suitable nanotubes length by changing the anodization time. The findings of this investigation are displayed in Figure 4.9. It is hereby also verified that, in KPF_6/EC:DEC electrolyte, the CE is lower than in KFSI/DME. In the former, the specific capacity follows a monotonous behaviour, with longer NTs on the top. By contrast, in ether electrolyte the behaviour is parabolic, with 15 min-grown NTs on the top, whereas 30 min- and 7.5 min-grown samples show inferior capacity. It could be attributed to a more difficult electrolyte wetting of the NTs internal walls, and consequently the longer nanotubes might not have the whole length involved in K^+ hosting. The difference in

the salt anion size might play an initial role, since FSI⁻ is roughly two times bigger [71] than PF₆⁻ [72]. However, other effects such as ion aggregation, ion mobility or charge accumulation and screening in the structure contribute to the permeation of the electrolyte. Also, the nanotubes diameter is reported to affect the ion absorption in NIBs with different electrolytes, effect that was not reported for LIBs: narrower NTs prevented Na$^+$ infiltration, which remained in the bulk electrolyte [73]. This might be the effect observed for longer nanotubes, where - due to the oxidation technique - their bottom diameter results smaller than the top [74].
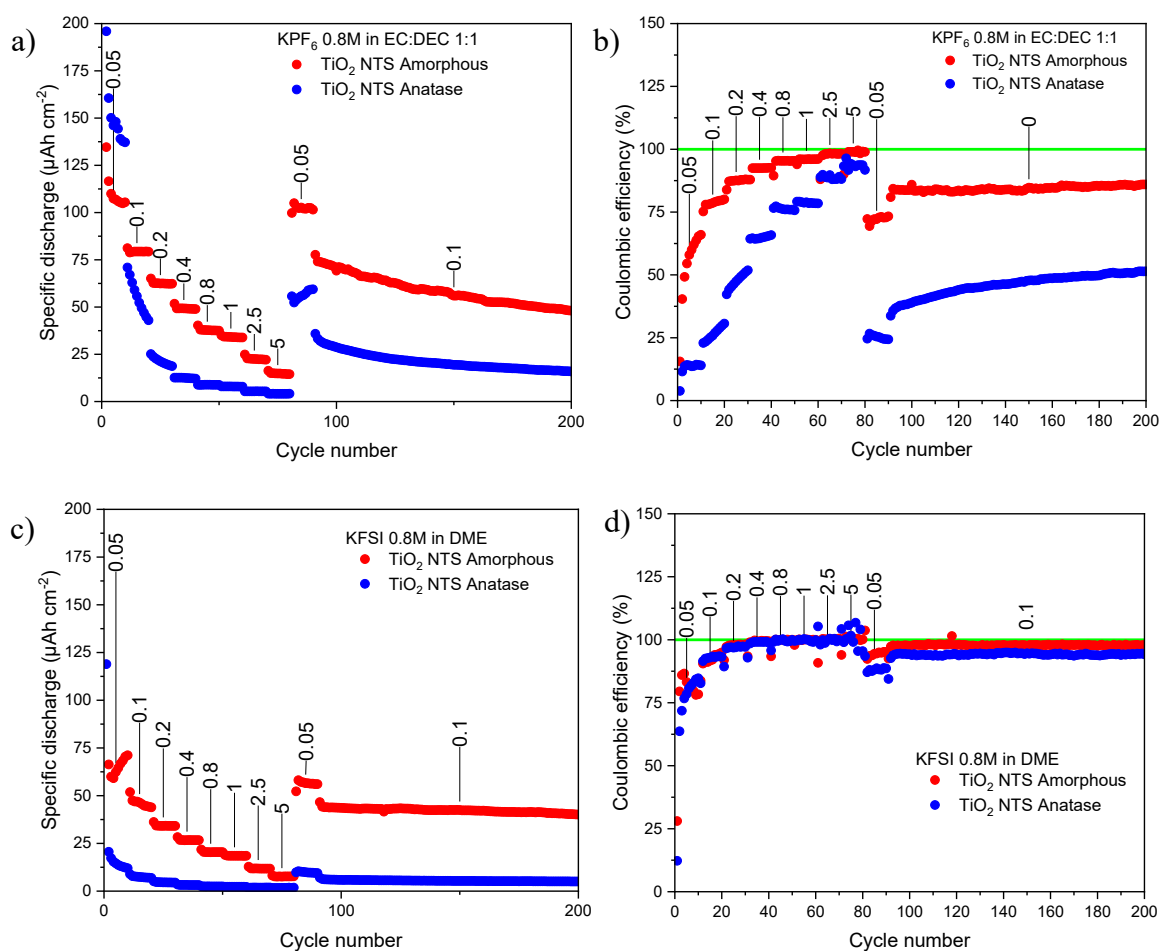
Figure 4.8: Comparison of TiO₂ NTs (15 min) electrodes at different current densities (mA cm^{-2}) with respect to crystalline phase and electrolyte. Specific discharge or CE *vs*. cycle number for KPF₆- (a, b) and KFSI-based (c, d) electrolytes .

58
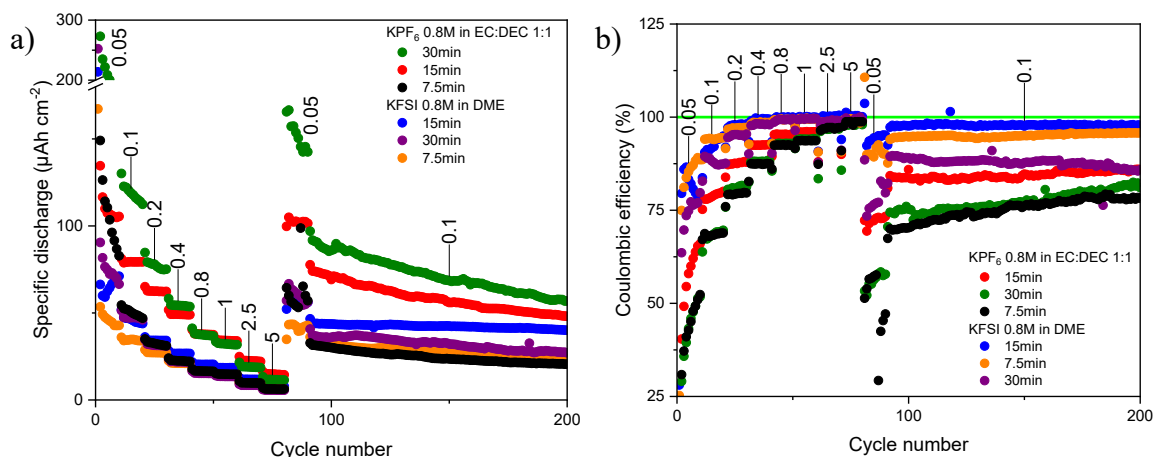
Figure 4.9: Comparison of TiO$_2$ amorphous NTs with different anodization times. a) Specific capacity and b) CE *vs.* cycle number at different current densities (mA cm^{-2}).

It is of interest to compare the performances of the TiO$_2$ anodes in order to understand which nanostructure better suits PIBs. The specific capacity is hereby normalized with respect to the active area of the electrode and regardless of its mass Figure 4.10. It is evident that KFSI/DME electrolyte capacity looks stable over prolonged cycling in all the tested systems, differently with what verified in KPF$_6$/EC:DEC. This second electrolyte, despite delivers higher capacities in the initial cycles, is affected by a progressive performance decline.

TiO$_2$ NPs 200 µm are characterized by higher discharge capacity, but it is not pure material due to the inclusion of 10% conductive carbon. It is also more performant than the correspondent 100 µm deposition, although it is because the total mass was neglected in the computation. Following these considerations, the most promising system is the TiO$_2$ NTs amorphous 15 min in KFSI/DME electrolyte, denoted by a very stable behaviour (Figure 4.10 a).
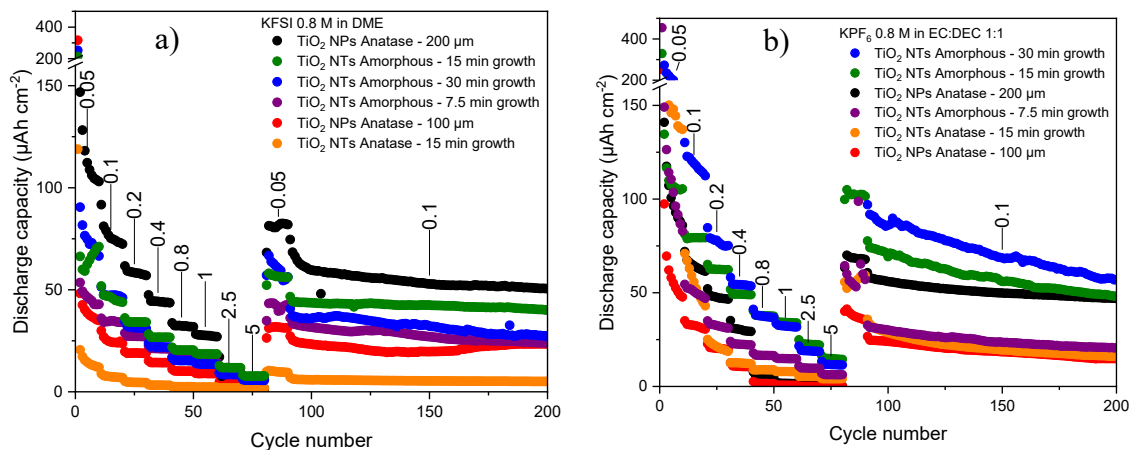
Figure 4.10: Comparison of the specific capacity per unit area of the TiO_2 electrodes in different electrolytes at different current densities (NTs: mA cm^{-2}, NPs: A g^{-1}).

4.2.1 Galvanostatic long cycling

The reliability of the cell over prolonged charges and discharges was tested under constant Figure 4.11 or variable Figure 4.12 current densities, until cell death. It happened at cycle 1722nd in the former and 981st in the latter. The remarkable difference existing among these lifetimes shows that damages coming from a fast intercalation reaction, despite being individually small, in the long run play a critical role in the early failure of the cell. However, the cells achieved a significant number of cycles, addressing that TiO_2 amorphous NTs are an interesting material in the PIBs field. In the constant-current aging Figure 4.11, the specific capacity retention with respect to cycle 15th was 93.0% (cycle 115th), 85.7% (cycle 215th), 76.2% (cycle 345th), 47.6% (cycle 1015th) and 31.0% (cycle 1715th), respectively. On the other hand, capacity retention in the variable-current aging Figure 4.12 with respect to cycle 25th was 69.1% (cycle 185th), 60.3% (cycle 345th) and 79.8% (cycle 825th), evaluated at 0.1 A g^{-1}. In the second case, despite at cycle 345th the capacity fade attained was larger, as cycling proceeded this fading slowed down and even improved, which was not observed in the constant-current long cycling. It is also noteworthy that in the first 20 cycles Figure 4.12 a steady capacity activation is shown, which could be the reason behind the capacity retention. Such an activation was observed in [75] for anatase TiO_2 nanotubes and attributed to a possible structure ordering upon cycling driven by the insertion of cations. It also proves that this capacity activation proceeds longer (for at least 20 cycles) than the 10 cycles at low C-rate of the normal

galvanostatic cycling performed in this thesis. This improvement was observed exclusively at low current densities because of the time required by this process, which makes it unlikely to occur employing more intense currents [76].

Charge/discharge curves are also presented to analyse the evolution of the voltage profile as cycling proceeds Figure 4.13. No evident voltage plateau could be identified, nonetheless the polarization is contained, suggesting that ion trapping inside the nanotubular framework is not a major concern. It is attributable to the amorphous crystalline phase, able to better accommodate large ion insertion/deinsertion without the excessive rigidity of anatase. The more flexible structure, caused by larger defects presence, prevents ions from remaining stuck.
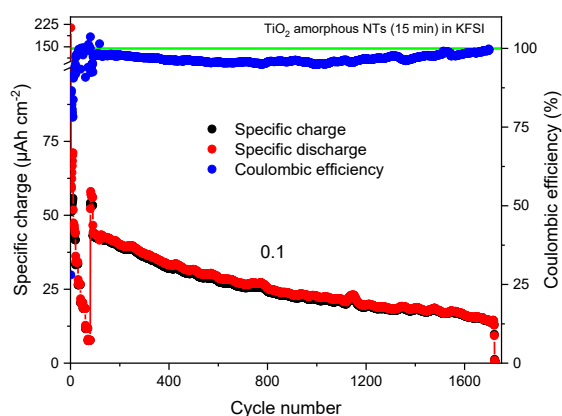
Figure 4.11: Long cycling of TiO_2 amorphous NTs at a constant current density (mA cm^{-2}) until death, occurred at cycle 1722nd.
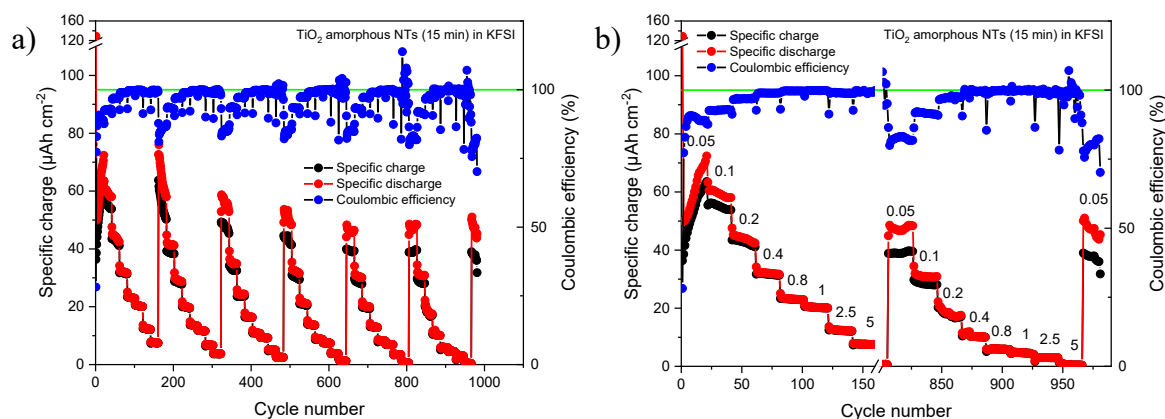
Figure 4.12: Long cycling of TiO_2 amorphous NTs in KFSI at different current ranges: a) Complete cycling; b) First and last 160 cycles. Current densities in (mA cm^{-2}).
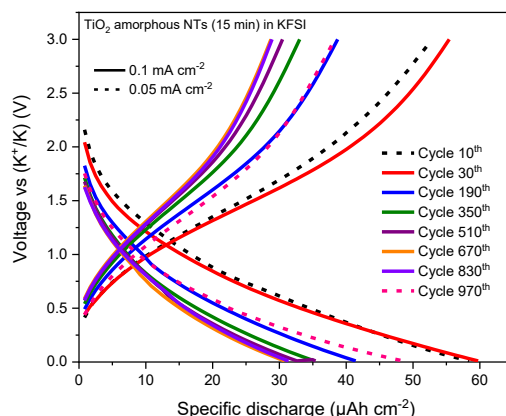
Figure 4.13: Charge/discharge curves of TiO$_2$ amorphous NTs in KFSI obtained during long cycling at variable current density.

4.2.2 Morphological analysis

The XRD results reported in Figure 4.14 are significative for the amorphous and anatase samples, reporting the pristine and cycled (potassiated and de-potassiated) electrodes. Alongside, the reference patterns for the anatase phase and the salt contained in the electrolyte are plotted, as well as the XRD result of the titanium foil on which NTs grew. The amorphous sample in a) does not present any characteristic peak associated to any of the TiO$_2$ crystalline structure, and no change was detected over repeated cycling. In the cycled electrodes a new peak at low diffraction angles appeared, but it was attributed to the residual presence of salt, coming from the electrolyte after drying. The same conclusion can be drawn for the anatase samples in b), where the appearance of new peaks is attributed to the salt and the presence or absence of intercalated K$^+$ ions does not affect the crystallinity. These results are in contrast to [77] and [67], in which a partial amorphization of the anatase lattice consequent to sodium ions insertion is depicted.
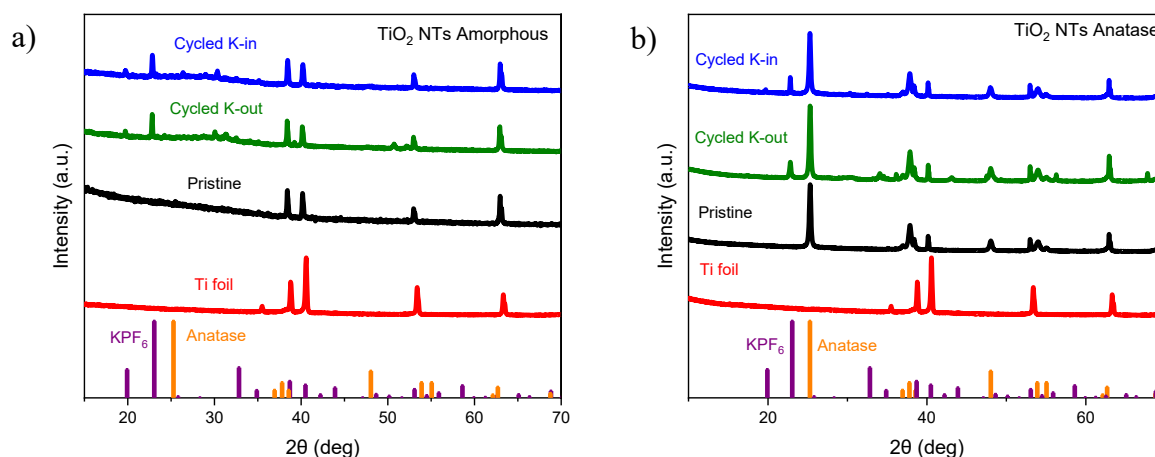
Figure 4.14: XRD patterns of TiO$_2$ NTs a) amorphous and b) anatase samples before cycling and cycled. The contribution of the titanium current collector and the reference patterns for the salt and the anatase crystalline phase are reported.

FESEM images reported in Figure 4.15 show the ordered structure of nanotubes in both their crystalline forms; the anatase (e-h) looks slightly more ordered, especially from the top view, than the amorphous structure (a-d). The average NT length associated to a 15 min growth was 6 µm, regardless the crystallinity, with an average diameter of 100-120 nm, affected at a ratio of approximately 2.5 nm V^{-1} by the anodization voltage [74]. The average wall thickness measured around 20 nm on top. Between cycled and pristine electrode, no relevant changes were detected, the nanotube entry remains open and the mechanical cohesion among them is preserved, as well as their integrity. Some electrolyte decomposition products or salt depositions can be observed in the cycled electrodes (c, d, g, h).
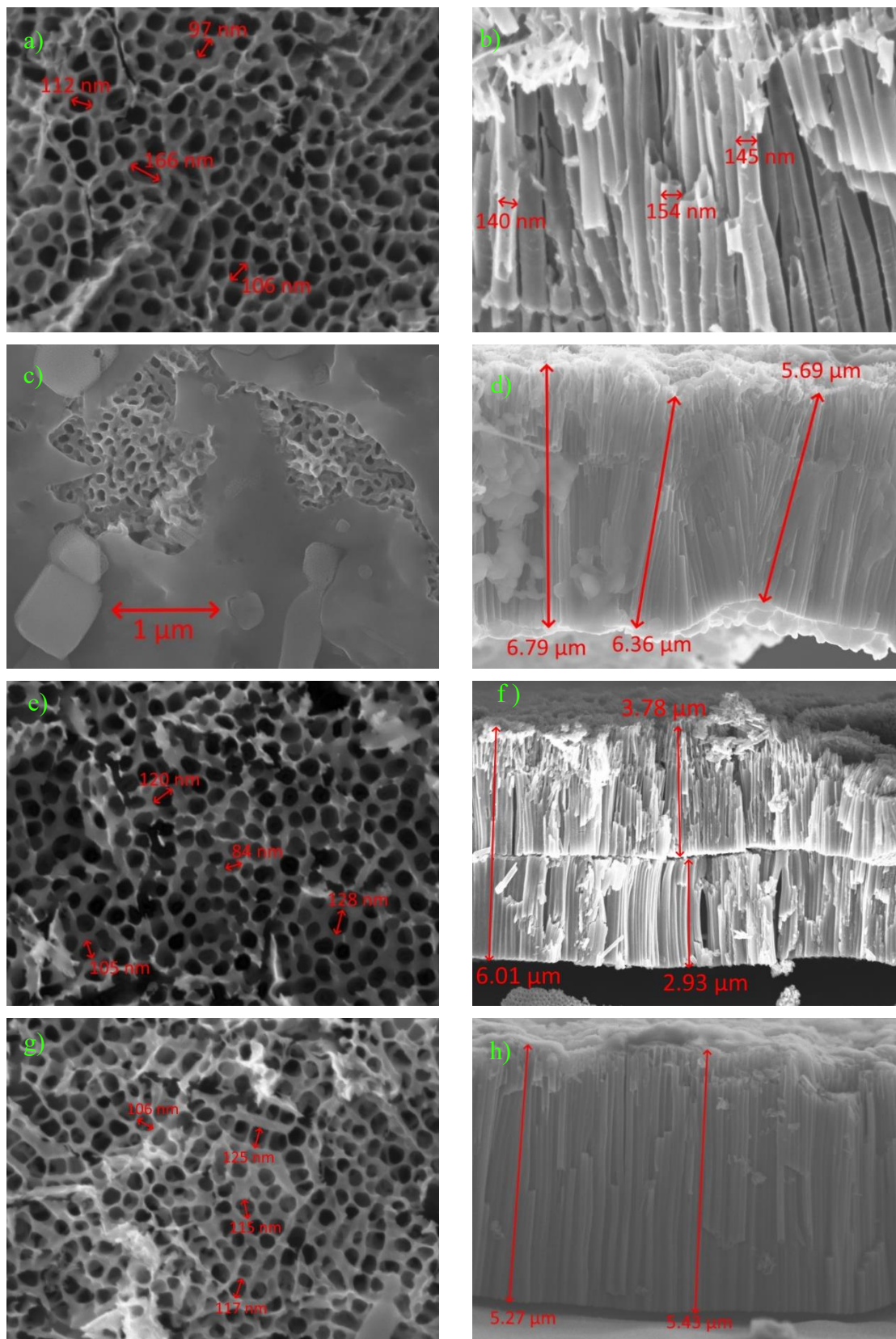
Figure 4.15: FESEM picture of NTs amorphous fresh (a, b), amorphous cycled (c, d), anatase fresh (e, f), anatase cycled (g, h) electrodes. (a, c, e, g) are in top-view, whereas (b, d, f, h) are in cross-section.

4.2.3 Cyclic voltammetry

The first cycle shown in Figure 4.16 presents several cathodic peaks that tend to disappear or reduce their intensity in the subsequent cycles. They witness the occurrence of irreversible reactions, typically attributed to the electrolyte decomposition of both salt and solvent at lower voltages, i.e. below 1 V [79, 76]. The insertion and deinsertion peaks, associated to a Ti^{4+}/Ti^{3+} redox reaction, are associated to the 0.81 and 1.21 V peaks, respectively. The extraction peak increases its magnitude during subsequent scans, in accordance with the activation behaviour observed in the galvanostatic cycling, and shifts towards slightly lower voltages. This rather broad peak is ascribed to the amorphous nanostructure, since a sharper peak was reported for the crystalline counterpart [75]. A similar change can be observed for the insertion peak, which does not increase its magnitude, but becomes broader.
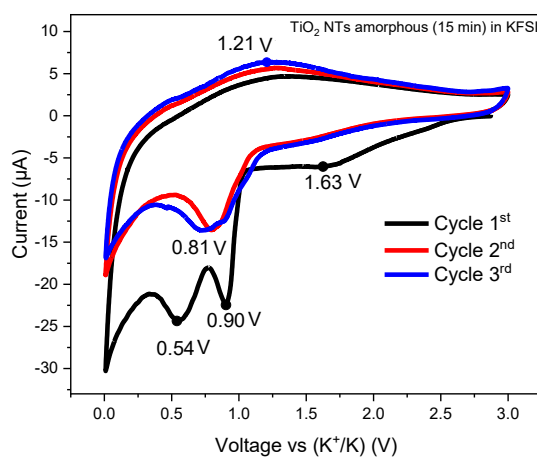
Figure 4.16: Voltammogram of the TiO_2 amorphous NTs sample in KFSI, 15 min growth.

4.2.4 Electrochemical impedance spectroscopy

Analysing the Nyquist's plot for TiO_2 amorphous nanotubes, some differences are evident with respect to the corresponding nanoparticles-based electrode. The equivalent circuit Figure 4.17 was modified by adding a R-CPE couple to reflect a second smaller semicircle, despite it is hardly noticeable into the inset of Figure 4.17. This further contribution was at first attributed to a passivation layer on the highly-reactive nanotube surface, that increases the system impedance causing additional losses [52]. By comparing the fresh and cycled electrode, a

decrease in the charge transfer resistance could reveal an improvement in the cation accommodation structure, as suggested by the first cycles in Figure 4.8, where an increase in the specific capacity was observed. However, this value is very high and could be representative of a slow ions kinetics at the electrode/electrolyte interface [78]. The electrolyte and connectors impedance, modelled by the high-frequencies system resistance R_1, remain relatively stable and at low values Table 4.4, which may reveal good system stability.
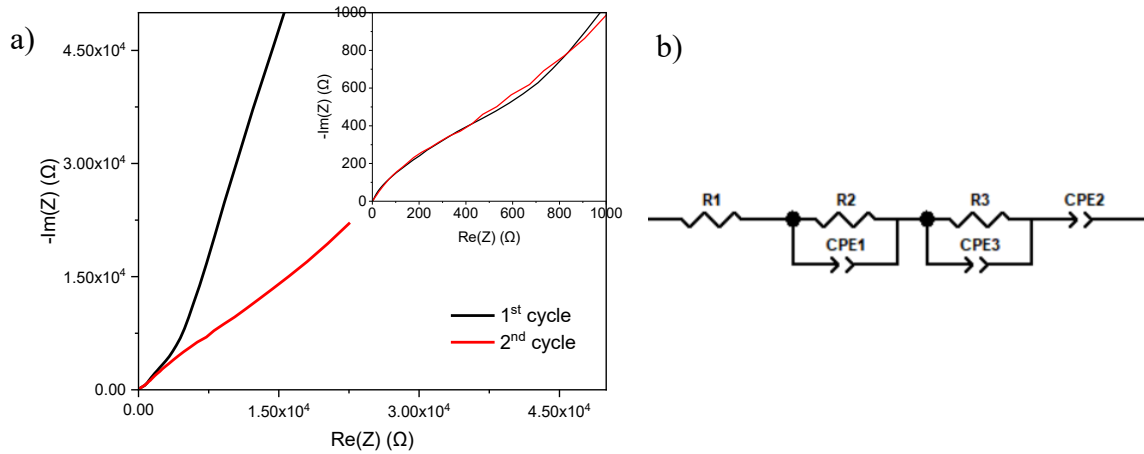
Figure 4.17: a) EIS results of TiO$_2$ NTs of the fresh cell and after the CV, the inset reports a narrower impedance window in the high frequency region. b) Equivalent circuit used as model to fit the data.

Table 4.4: Results of the fitting of TiO$_2$ NTs based on the equivalent circuit.

		R_1	R_2	R_2
Fresh	Value (Ω)	2.63	2740	454
	Error (%)	-	21.6	15.9
After CV	Value (Ω)	6.26	893	464
	Error (%)	-	62.6	16.0

4.2.5 Mott-Schottky's analysis

Following the equation (3.12), the donor density was computed, considering the dielectric constant equal to 38 for amorphous and 50 for anatase TiO_2 [66]. The specific capacitance *vs.* electrode potential is reported in Figure 4.18 for the optimal frequencies and the results are reported in Table 4.5, demonstrating consistency to what was already reported by other authors [55, 67, 81]. The choice of the frequency for the study is reported in Annex II.

The higher potential bending present in the amorphous phase is reflected in the donor density at the oxide surface, being three times bigger than in the anatase phase. A high N_D improves the charge conductivity of the material, therefore enhancing its electrochemical performances [55]. The worse behaviour of the anatase phase reported in Figure 4.8 can be partially ascribed to this fact. The reduction in the donor density could also come from a smaller number of defects consequent to the crystalline rearrangement provided by the annealing. Besides, the anodization technique in a F⁻-rich electrolyte was reported to introduce other chemical species that can act as defects and are then eliminated through the heat treatment [66]. Indeed, higher donor densities generally characterize nanostructures formed in chloride/fluoride solutions [79], partially explaining the differences observed between anatase nanotubes and nanoparticles.

Table 4.5: Results of the Mott-Schottky's analysis for TiO_2 nanotubes. The results for TiO_2 NPs are also reported for comparison.

	TiO₂ amorphous NTs	TiO₂ anatase NTs	TiO₂ anatase NPs
Flat-band potential	1.6	1.8 V	1.55 V
Donor density (cm⁻³)	6.69×10^{22}	2.06×10^{22}	3.83×10^{19}
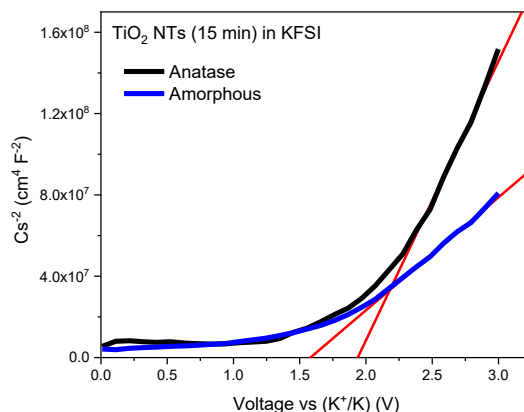
Figure 4.18: Mott-Schottky's plots for TiO_2 nanotubes. The slope of the linear portions is 5.55 $\times 10^7 \, cm^4 \, F^{-2} \, V^{-1}$ for amorphous and $1.37 \times 10^8 \, cm^4 \, F^{-2} \, V^{-1}$ for anatase.

4.3 Prussian blue nanoparticles

The cathodic material was tested in the voltage range between 2 and 4 V, in a similar manner to the anodic one, evaluating the impact of a thicker or thinner electrode on its performances. Both the configurations were tested employing two electrolytes. It is worth noticing that the cell with 100 µm-thick electrode, cycled in KFSI/DME electrolyte, was not able to fulfil the cycling program. It happened with more than one cell, hence it was attributed to the corrosion of the aluminium current collector from an imide-based electrolyte [80]. Interestingly, this phenomenon was not shown by 200 µm-thick electrodes cycled in the same electrolyte, perhaps due to the protection provided by a bulkier layer of active material. It is also noteworthy that the rate capability of such a configuration is higher than the corresponding one cycled in KPF_6/EC:DEC electrolyte, which showed almost the same specific capacity in the final aging Figure 4.19, but poorer performances at higher C-rate. It might be ascribed to a slower ions transfer kinetics in a carbonate-based electrolyte, that encounter a thicker and less-stable SEI layer that hampers their fast insertion in the framework.

Substantial inconsistences exist among the specific capacity obtained in the literature, because of the sensitivity of PBA to defects, such as vacancies and residual water [81] trapped in the lattice. Because of the large variety of synthesis methods, as well as precipitation conditions and drying parameters, it is generally difficult to compare the results, even if obtained with very similar compounds [82].
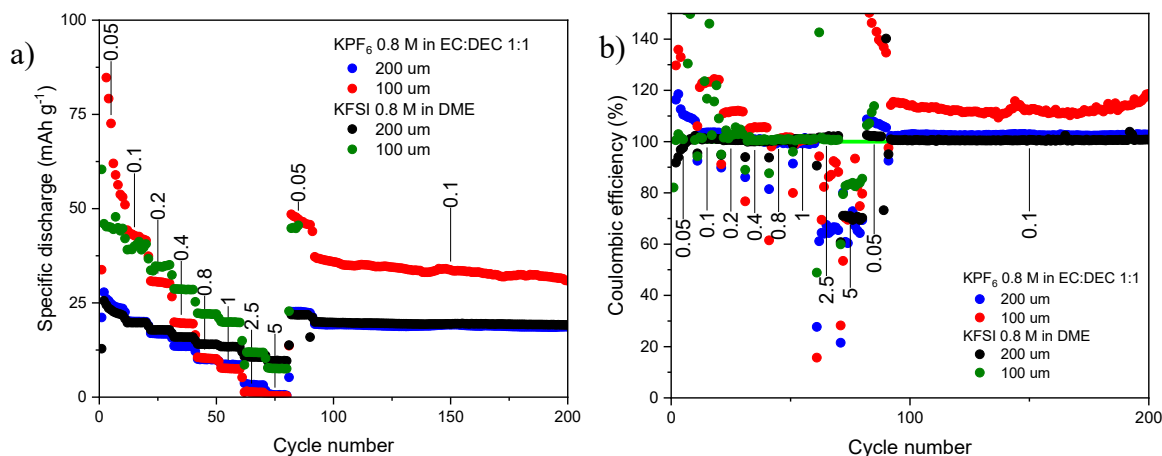
Figure 4.19: Comparison of PB NPs electrodes at different current densities (A g⁻¹) with respect to thickness and electrolyte. Specific discharge (a) or CE (b) *vs*. cycle number.

4.3.1 Galvanostatic long cycling

Second-step analyses were carried on the 200 µm-thick sample, coupled with the KFSI/DME electrolyte. Its choice was driven by the stability and the high Coulombic efficiency (close to 100%) previously demonstrated. Thus, performance assessment during long cycling until failure of the cell are here presented, employing both a constant and a variable current density as explained in the chapter "Experimental procedures and methods". Despite the cell was able to survive 2170 cycles Figure 4.20, after approximately 1000 cycles some degradation process took place, showing a Coulombic efficiency different than 100%. However, these reactions do not seem to be destructive, since their duration exceeded 1100 cycles, slightly affecting the capacity of the cell. Capacity fading was indeed contained, retaining 92.8% after 500 cycles, 89.8% after 100 cycles and 79.7% after 2000 cycles, showing a Coulombic efficiency of 100% in the first 1000 cycles. Moreover, the charge/discharge curves can be almost perfectly overlapped and the operating voltage plateau, centered at about 3.5 and 3.1 V, is in good accordance with the CV results.

The rate capability was also tested, the results of which are shown in Figure 4.21, unveiling the poor performances at high current densities, with the cell almost unable to complete the charge/discharge. Big K^+ ions are incapable of reaching the active sites of intercalation, perhaps due to the slow diffusion because of their size, together with defects abundance [83] that could

slow down ion movement. Nevertheless, the capacity fading was negligible despite the intense cycling, recovering the 99.7% of capacity (cycle 15th *vs*. cycle 665th). The cell failure was induced at cycle 805th and the progressively lower CE suggests the starting of the degradation progress observed in constant current cycling.
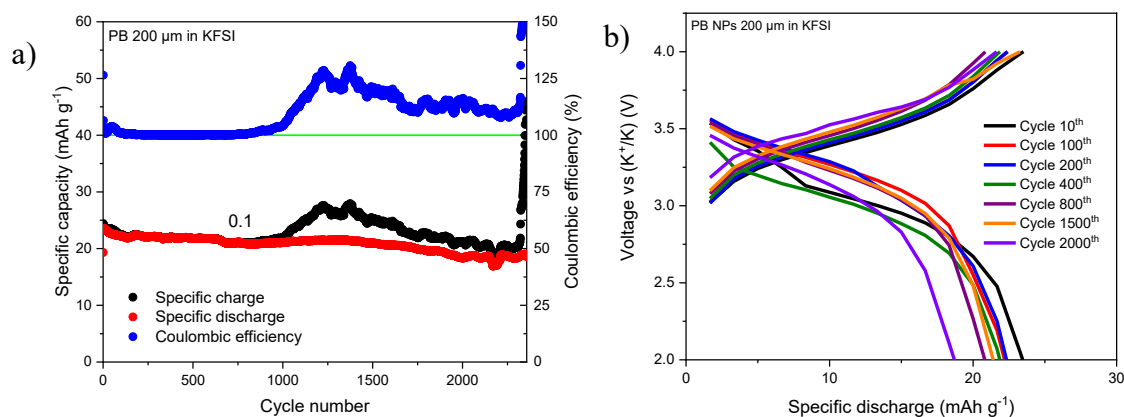
Figure 4.20: a) GC of PB 200 µm at constant current density (0.1 A g⁻¹) until failure. b) Charge/discharge profiles during cycling.
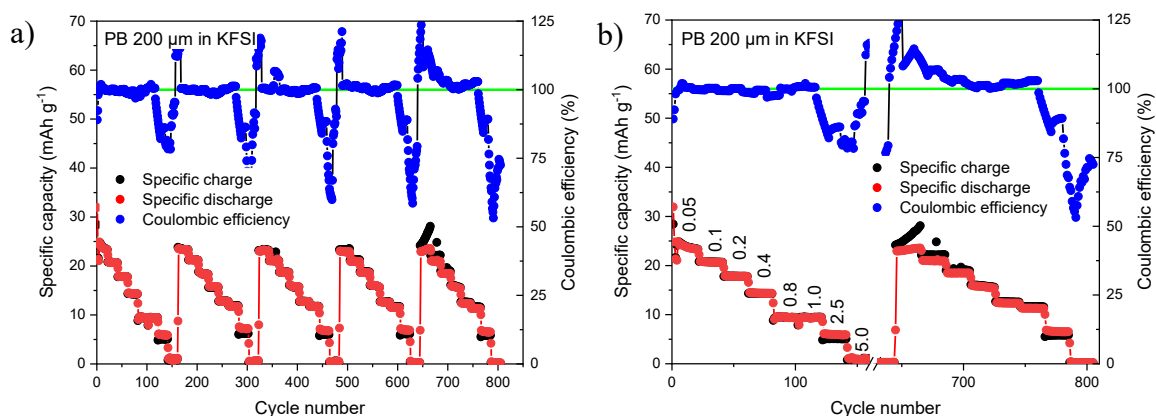
Figure 4.21: GC at variable current density (A g⁻¹), 20 cycles each: a) full cycling, b) first and last 160 cycles.

4.3.2 Morphological analysis

From the FE-SEM analysis of this electrode, the nanoparticles size observed was in the micron-scale range (Figure 4.22 a), that means a longer diffusion path compared to the typical nano-scale range of nanoparticles [84]. A longer diffusion path is translated in poorer bulk material utilization, originating the bad rate capability observed in Figure 4.21, where ions do not have enough time to reach the active hosting sites.

By comparing the pristine and cycled electrodes (Figure 4.22 b, c), the similarity between the structure and the particles size is noticeable. It highlights the framework preservation, perhaps due to the contained volume retention of PBAs, which does not damage the structure. However, products deposited on the electrode surface of the cycled electrode suggest that some irreversible reaction occurs, which may lead to the lower Coulombic efficiency achieved after cycle 1000th shown in Figure 4.20.

FE-SEM analysis revealed also the reaction occurring between PB and the aluminium current collector, further analysed in Annex III.

a)
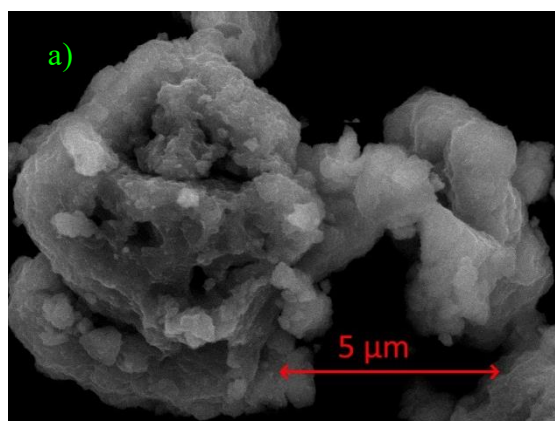
c)
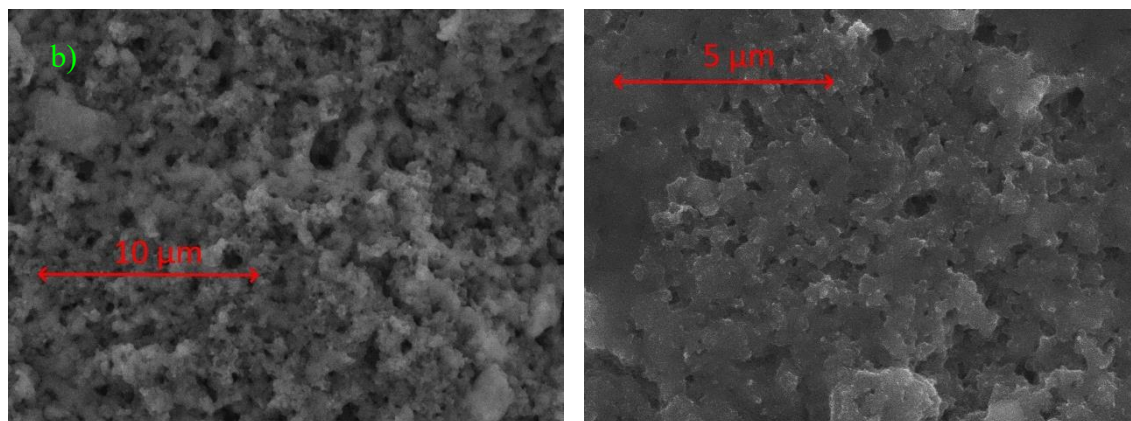
Figure 4.22: FE-SEM images of PB electrode: a) powder, b) fresh electrode, c) cycled electrode.

4.3.3 Cyclic voltammetry

In the operating voltage range, a single redox couple (3.42 and 3.14) associated to the low-spin Fe^{3+}/Fe^{2+} couple was observed, which is in contrast with the two-step intercalation behaviour observed in some PBA [84], but confirms the single plateau shown in the charge/discharge curves reported in (Figure 4.20 b). This second insertion is generally hardly achievable in non-aqueous electrolytes because it occurs at higher potential which are beyond their safety window, resulting in electrolyte decomposition [2]. It was reported in [85] and [86] the second redox peaks at 4.16/3.91 and 4.13/3.95V respectively, therefore slightly out of the analysed window. Conversely, the first insertion is in good accordance with the one found at 3.42/3.14 V. It is noteworthy the symmetry of those two peaks, that share almost the same magnitude and area, suggesting the good reversibility of the reaction [41].

It was reported that, for Fe-HCF, insertion voltage increases with the ionic radius of inserted cations, because it is more favourable in body-centered sites rather than face-centered, given the larger available space [87]. However, this site is more energetic that the face-centered, resulting in an insertion voltage that is higher than in Li^+ or Na^+ counterparts and with stabler reaction products. By contrast, bigger ions, such as K^+, can suffer from slower diffusion than smaller ones, such as Li^+, which can lower the rate capability and the specific capacity. Interestingly, the positive effect on the voltage overcomes the negative on the capacity, favouring the energy density of batteries that employ elements with larger ionic radius [82].
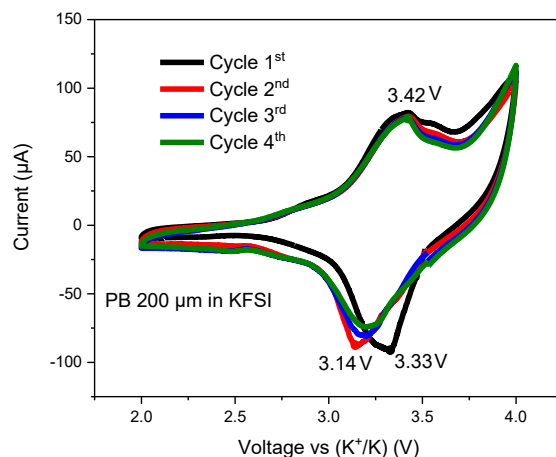
Figure 4.23: Voltammogram of the PB NPs 200 µm sample in KFSI.

4.3.4 Electrochemical impedance spectroscopy

EIS was carried to investigate the surface impedance of the fresh and cycled cell, in order to quantify its evolution. The results are plotted in Figure 4.24 and modelled with the circuit shown. R_1 is representative of the ion transport in the electrolyte and connectors resistance, and it is noticeable that its value remains almost constant, which confirms stability. By contrast, the charge transfer resistance, modelled through R_2, undergoes a relevant increase, demonstrated by the larger depressed semicircle in the medium-frequencies region [88]. It might be caused by some irreversible reactions that cause the peak at 3.33 V in the CV to shift towards lower voltages. It proves a more difficult ions penetration in the electrode material as cycle proceeds, suggesting that some reaction products deposited on the surface hinder their passage from the electrolyte to the active material. Again, due to the roughness of the nanoparticulate morphology, CPE are preferred over pure capacitors to model the double layer capacitance.
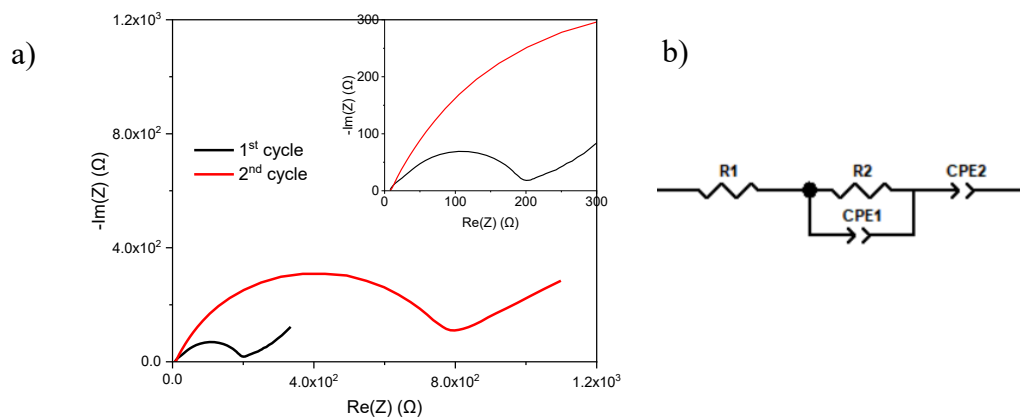
Figure 4.24: a) PB electrode EIS results of the fresh cell and after the CV. b) Equivalent circuit used as model to fit the data.

Table 4.6: Results of the fitting of PB NPs based on the equivalent circuit.

		R_1	R_2
Fresh	Value (Ω)	7.63	195.5
	Error (%)	-	1.41
After CV	Value (Ω)	7.98	720.2
	Error (%)	-	0.64

5 Aim of the work and future prospects

This thesis was devoted to the investigation of some electrode materials for potassium-based batteries. This technology is currently under exploration in research centres around the world, being at its infant stage. Given its possible applications in stationary energy storage systems, that are critically needed in the fight against climate change, a further comprehension and development is urgently required. At today state-of-the art, several issues were identified, lots of them already addressed in the more developed LIBs. Nonetheless, proper solutions are still missing, demanding for a broader identification of new materials and more precise characterization of existing ones.

In this optic, titanium dioxide was examined because it is a well-known material, largely available, cheap and environmentally friendly. Considering the attention to sustainability that the new technologies should pay, and the cost-reduction needed in order to implement batteries in the smart grids of the future, it could be a really interesting choice. On the other hand, its characterization in PIBs lies in such an early stage that obtaining compelling results would have been quite optimistic. Nonetheless, the outcomes presented in this thesis highlight the importance of the morphology and the crystalline phase, addressing the amorphous nanotubes as the best solution among the studied. The importance of defects to alleviate residual stress and shorten the diffusion path in the bulk material to fasten the intercalation/deintercalation reaction were addressed as research-worthy directions because of the large potassium size. Some promising results, coming especially from the stability, were obtained. The simplicity of the synthesis technique and the absence of any conductive carbon additive justify future structural optimizations following these paths.

The study and comprehension of cathode materials still lie far behind the anode in the research panorama. Hence, the Prussian blue was studied because of the interest shown in academic papers toward this substance. Its low cost and high operational voltage are the main features that outline PB as a possible successful cathode to design a cost-effective and energy-dense battery for grid applications. Alongside, the successful employment of aluminium as a current collector, also coupled with imide-based electrolyte (although the corrosion issue shown in other works), pushes forward both the stability and the cost reduction of the cell. What emerged is the requirement of identification of a standardized synthesis and drying method for the

powder, able to decrease the amount of water trapped in the crystalline lattice that reduces the active sites for cation hosting. A suitable synthesis method must be defined also to tune the size of PB nanoparticles, aimed at reducing the diffusion path for K^+ and increasing the total surface by decreasing their dimensions. Moreover, the material here analysed was the Fe-HCF, but the crystalline structure is shared between other members of this family of compounds, such as Mn-HCF. Thus, another suitable optimization path for future works would be to change the metal redox centres.

The importance of the electrolyte and its impact on each material was a relevant part of this thesis too. Thanks to the results obtained, KFSI-based electrolyte proved to deliver better and stabler performances in every system analysed, achieving a Coulombic efficiency really close to 100%. However, there is room for improvement in this field, , since the concentration of salt is of primary relevance in determining the cell performances, as well as the inclusion of some additive to improve stability and rate capability.

Annexes

Annex I: C65 impact on TiO$_2$ NPs

By looking at (Figure 4.5 b), it can be noticed that the de-insertion peak shown by the material at 1.46 V tends to disappear after 100 cycles. Hence, pushed also by the very good performances obtained by carbonaceous compounds [89], the impact of the C65 additive on the cell capacity was estimated.

In order to estimate the fraction of capacity delivered by the conductive carbon and by the active material, respectively, two methods were used. They are based on the same experimental configuration, i.e. one cell with the composition reported in Table 3.1 and one made out exclusively of C65 and binder, as reported in Table 6.1. The first approach compares the capacity delivered by the two cells after 100 cycles in order to understand each contribution, following eq. (6.1),(6.2). In the equation, C_{TiO2} is the capacity provided by the titanium dioxide alone, C_{TOT} is the capacity of the cell, while C_{C65} is the capacity of the carbon additive cell alone (Figure 6.1 a). 0.11 and 0.89 are the relative amounts of TiO$_2$ and C65 without considering the mass of the binder, because it does not provide any capacity.

The second approach compares the area enclosed in their voltammogram, being a graphical representation of the capacity. Concerning the latter, the area of C65 was normalized with respect to the ratio of carbon between the two cells (3.69) (Figure 6.1 b).

$$C_{TOT} = C_{Cell} * (m_{TiO_2} + m_{C65}) \qquad (6.1)$$

$$C_{TiO_2} = (C_{TOT} - C_{C65} * 0.11)/0.89 \qquad (6.2)$$

Comparing the results it is clear that the impact of the carbon additive was not negligible at all: from the first method it resulted that it delivered the 84% of the capacity, while from the second it delivered the 66%. Despite the two results do not provide the same result, given the rough nature of the procedure, the large majority of the capacity could be ascribed to the conductive carbon even though its weight fraction was only 10%. Supported by this conclusion, the

nanotubes-based electrode was preferred over the nanoparticles-based one, although from Figure 4.10 the second emerged as characterized by larger specific capacity.

Table 6.1: Composition of the carbonaceous electrode.

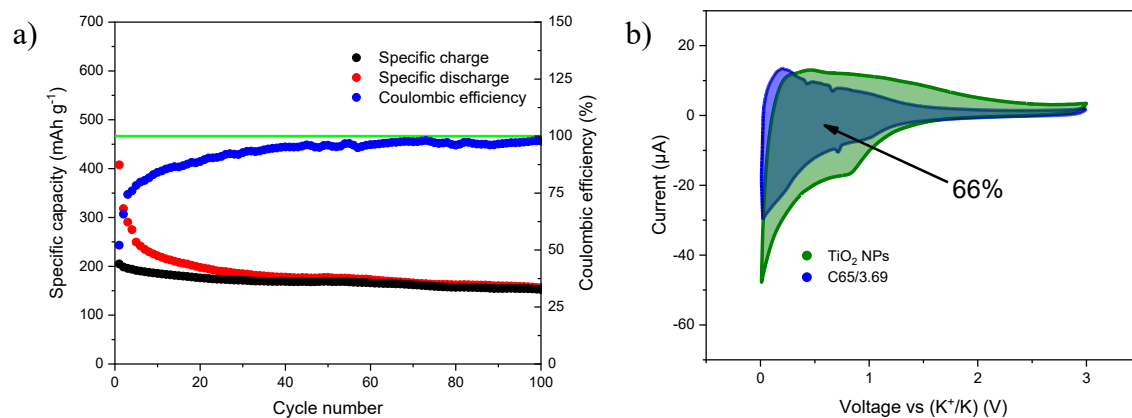| *Ingredient*	*Commercial product*	*Content*	*Mass (g)*
Carbon additive	C65	80 wt%	0.00072
Binder	PVDF	20 wt%	0.00018

Figure 6.1 a) Charge/discharge curves of the C65 cell at 0.1 A g^{-1}. b) Voltammogram comparison of the two cells.

Annex II: Frequency selection for Mott-Schottky's analysis

The Mott-Schottky's equation requires the presence of capacitive behaviour in order to be applied. Hence, the analysis is carried at every frequency in a defined range, i.e. 100 kHz - 10 mHz, but the number of donors is computed from the results obtained in only one of them. In order to select it properly, a capacitive behaviour should be identified, which can be done through the Bode's plot (impedance module and phase angle *vs*. frequency).

If the behaviour is dominated by capacitive effects, the capacitance module approaches the impedance module (6.3), which identifies a linear equation in the logarithmic plot impedance module *vs*. frequency with a slope of -1. It is therefore a first hint of the space charge redistribution on the semiconductor surface.

$$\log|Z| \cong \log|X_c| = \log\frac{1}{\omega C} = -\log C - \log\omega \qquad (6.3)$$

Alongside, in a pure capacitor, there is an angular delay of -90° between the voltage and the current. It follows that the interface capacitance dominant effect is larger as the phase angle in the Bode's plot becomes closer to this value. The Bode's plots of each semiconductor electrode are reported in Figure 6.2, where the region of frequencies closer to a phase angle of -90° is highlighted and summarized in Table 6.2.

Table 6.2: Chosen frequencies for the Mott-Schottky's analysis.

Semiconductor	*log(f)*	*Frequency*
TiO$_2$ anatase nanoparticles	2.56	367 Hz
TiO$_2$ anatase nanotubes	-1.5	32 mHz
TiO$_2$ amorphous nanotubes	0.84	6.9 Hz
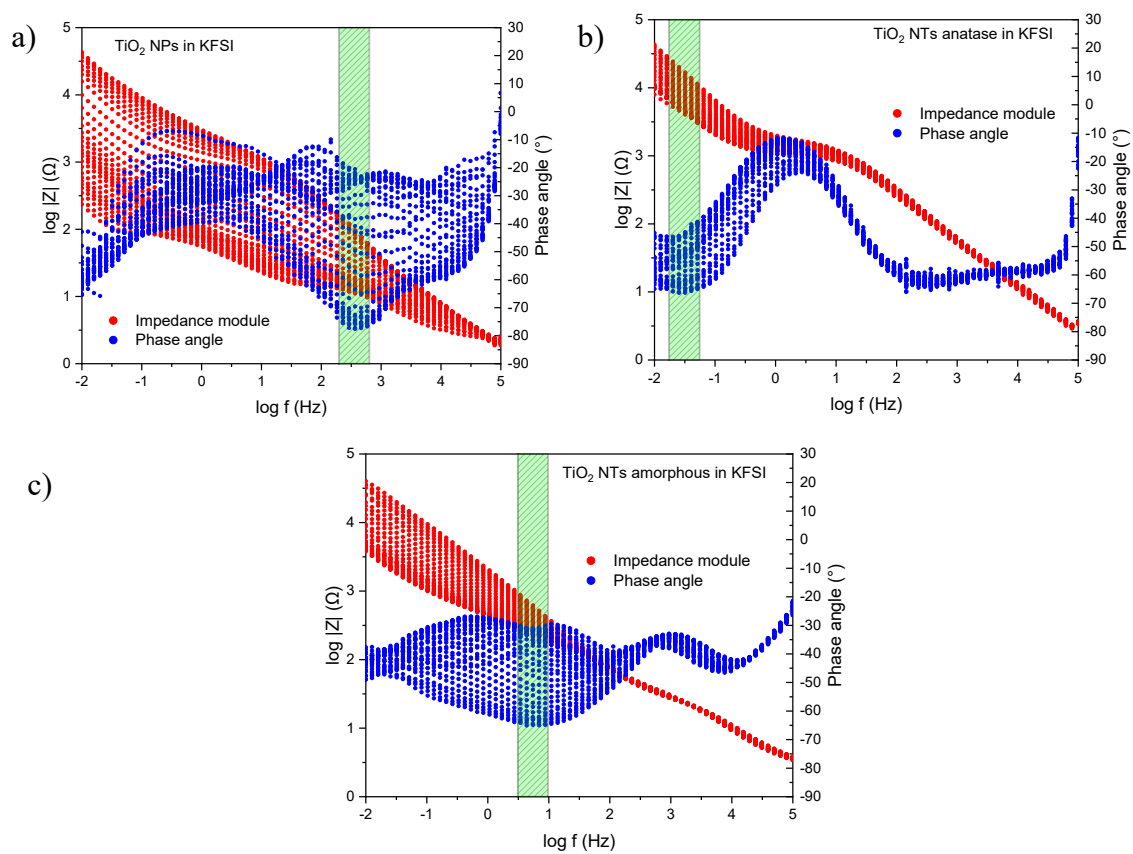
Figure 6.2: Bode's plots for TiO$_2$ NPs (a), NTs anatase (b), NTs amorphous (c).

Annex III: Current collectors in PB electrode

Because of the bulky conglomerates observed in the FESEM images of the PB electrode, and given their reference absence in the literature, further characterizations were carried out. First of all, an EDX test, aimed at identifying their composition, was done, and the results are reported in Figure 6.3. It came out that such conglomerates contained aluminium, confirming the formulated hypothesis and explaining why nothing similar was observed into the powder before slurry deposition onto the current collector. They were observed regardless the layer thickness. By the way, their impact on the material performances are still unclear because the operation of the cell was not hampered. Still, some reaction on the surface is induced because of the branched structures that can be observed in Figure 6.4, not present on the pristine electrode surface. The same slurry was deposited in the same way on a copper current collector Figure 6.5, without showing any conglomerate and with a more homogeneous surface. Nonetheless, because of the decomposition of copper at voltages beyond 4 V, the cells that employed this material as cathodic current corrector were not able to survive neither the first cycle.

Figure 6.3: EDX analysis of a conglomerate onto the PB electrode surface.

Figure 6.4: FESEM images of PB electrode, focus on Al-based compound: a) fresh electrode, b) cycled electrode.

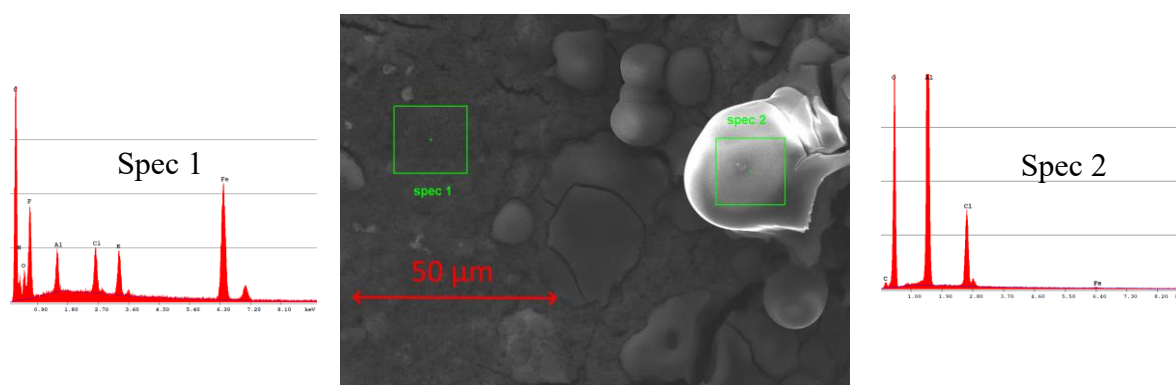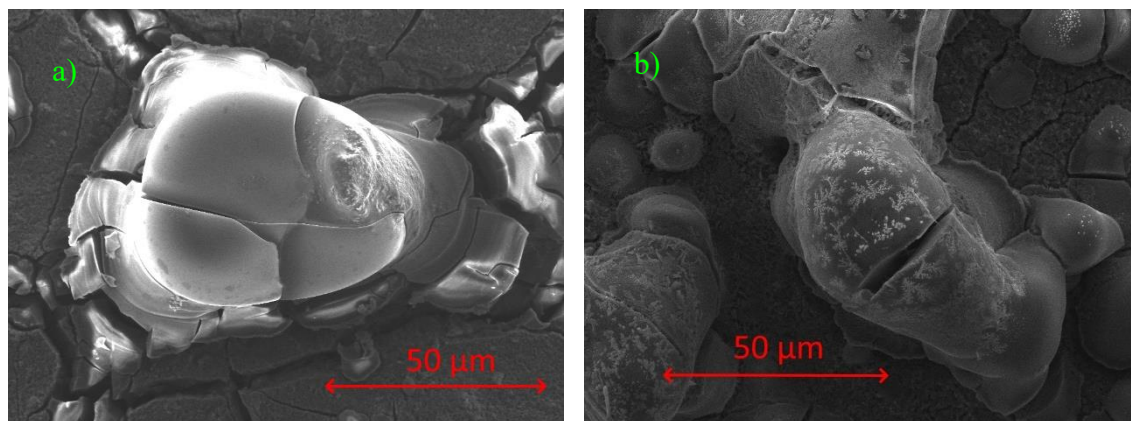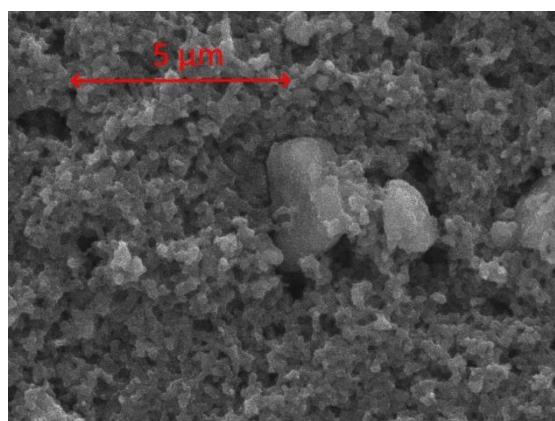Figure 6.5: FESEM image of the pristine PB electrode deposited on a copper current collector.

Bibliography

[1] IEA, "Energy Technology Perspectives 2020," https://www.iea.org/reports/energy-technology-perspectives-2020, Paris, 2020.

[2] IEA, "Global Energy & CO2 Status Report 2019," https://www.iea.org/reports/global-energy-co2-status-report-2019, Paris, 2019.

[3] J. E. Bistline and G. J. Blanford, "The role of the power sector in net-zero energy systems," *Energy Clim. Change,* vol. 2, 100045, 2021.

[4] J. E. Bistline and G. J. Blanford, "Impact of carbon dioxide removal technologies on deep decarbonization of the electric power sector," *Nat. Commun.,* vol. 12, no. 1, pp. 1-12, 2021.

[5] G. Plessmann and P. Blechinger, "How to meet EU GHG emission reduction targets? A model based decarbonization pathway for Europe's electricity supply system until 2050," *Energy Strategy Rev.,* vol. 15, pp. 19-32, 2017.

[6] J. D. Jenkins, M. Luke and S. Thernstrom, "Getting to zero carbon emissions in the electric power sector," *Joule,* vol. 2, no. 12, pp. 2498-2510, 2018.

[7] P. Siano, "Demand response and smart grids—A survey," *Renewable Sustainable Energy Rev.,* vol. 30, pp. 461-478, 2014.

[8] M. I. Alizadeh, M. P. Moghaddam, N. Amjady, P. Siano and M. K. Sheikh-El-Eslami, "Flexibility in future power systems with high renewable penetration: A review," *Renewable Sustainable Energy Rev.,* vol. 57, pp. 1186-1193, 2016.

[9] L. Bird, D. Lew, M. Milligan, E. M. Carlini, A. Estanqueiro, D. Flynn, E. Gomez-Lazaro, H. Holttinen, N. Menemenlis, A. Orths, P. B. Eriksen, J. C. Smith, L. Soder, P. Sorensen, A. Altiparmakis, Y. Yasuda and J. Miller, "Wind and solar energy curtailment: A review

of international experience," *Renewable Sustainable Energy Rev. ,* vol. 65, pp. 577-586, 2016.

[10] M. Arbabzadeh, R. Sioshansi, J. X. Johnson and G. A. Keoleian, "The role of energy storage in deep decarbonization of electricity production," *Nat. Commun.,* vol. 10, no. 1, pp. 1-11, 2019.

[11] D. Rastler, "New demand for energy storage," *Elec. Perspect.,* vol. 33, no. 33, pp. 30-47, 2008.

[12] B. P. Roberts and C. Sandberg, "The role of energy storage in development of smart grids," *Proc. IEEE,* vol. 99, no. 6, pp. 1139-1144, 2011.

[13] M. Manbachi, "Chapter 5 - Impact of Distributed Energy Resource Penetrations on Smart Grid Adaptive Energy Conservation and Optimization Solutions," in *Operation of Distributed Energy Resources in Smart Distribution Networks*, Academic Press, 2018, pp. 101-138.

[14] D. M. Davies, M. G. Verde, O. Mnyshenko, Y. R. Chen, R. Rajeev, Y. S. Meng and G. Elliott, " Combined economic and technological evaluation of battery energy storage for grid applications," *Nat. Energy,* vol. 4, no. 1, pp. 42-50, 2019.

[15] B. Wang, E. H. Ang, Y. Yang, Y. Zhang, M. Ye, Q. Liu and C. Li, "Post-Lithium-Ion Battery Era: Recent Advances in Rechargeable Potassium-Ion Batteries," *Chemistry - A European Journal,* vol. 27, no. 2, pp. 512-536, 2021.

[16] Z. Wu, J. Zou, S. Chen, X. Niu, J. Liu and L. Wang, "Potassium-ion battery cathodes: Past, present, and prospects," *Journal of Power Sources,* vol. 484, 229307, 2021.

[17] P. Hundekar, S. Basu, X. Fan, L. Li, A. Yoshimura, T. Gupta and N. Koratkar, "In situ healing of dendrites in a potassium metal battery," *Proceedings of the National Academy of Sciences,* vol. 117, no. 11, pp. 5588–5594, 2020.

[18] W. Zhang, J. Yin, W. Wang, Z. Bayhan and H. N. Alshareef, "Status of rechargeable potassium batteries," *Nano Energy,* 2021.

[19] V. Anoopkumar, B. John and T. D. Mercy, "Potassium-Ion Batteries: Key to Future Large-Scale Energy Storage?," *ACS Appl. Energy Mater. ,* vol. 3, no. 10, pp. 9478-9492, 2020.

[20] R. Borah, F. R. Hughson, J. Johnston and T. Nann, "On battery materials and methods," *Mater. Today Adv.,* vol. 6, 100046, 2020.

[21] Y. An, H. Fei, G. Zeng, L. Ci, B. Xi, S. Xiong and J. Feng, "Commercial expanded graphite as a low–cost, long-cycling life anode for potassium–ion batteries with conventional carbonate electrolyte," *J. Power Sources,* vol. 378, pp. 66-72, 2018.

[22] Z. Wang, S. M. Selbach and T. Grande, "Van der Waals density functional study of the energetics of alkali metal intercalation in graphite," *RSC Adv.,* vol. 4, no. 8, pp. 3973–3983, 2014.

[23] Y. Kim, Y. Park, N. S. Choi, J. Kim, J. Lee, J. H. Ryu, S. M. Oh and K. T. Lee, "An amorphous red phosphorus/carbon composite as a promising anode material for sodium ion batteries," *Adv. Mater.,* vol. 25, no. 22, pp. 3045–3049, 2013.

[24] J. Xu, S. Dou, X. Cui, W. Liu, Z. Zhang, Y. Deng and Y. Chen, "Potassium-based electrochemical energy storage devices: Development status and future prospect," *Energy Storage Materials,* pp. 85-106, 2020.

[25] Q. Wang, X. Zhao, C. Ni, H. Tian, J. Li, Z. Zhang and Y. Xu, "Reaction and capacity-fading mechanisms of tin nanoparticles in potassium-ion batteries," *J. Phys. Chem.,* vol. 121, no. 3, pp. 12652–12657, 2017.

[26] I. Sultana, M. M. Rahman, J. Liu, N. Sharma, A. V. Ellis, Y. Chen and A. M. Glushenkov, "Antimony-carbon nanocomposites for potassium-ion batteries: Insight into the failure mechanism in electrodes and possible avenues to improve cyclic stability," *J. Power Sources,* vol. 413, pp. 476–484, 2019.

[27] Q. Liu, L. Fan, R. Ma, S. Chen, X. Yu, H. Yang and B. Lu, "Super long-life potassium-ion batteries based on an antimony@carbon composite anode," *Chem. Commun.,* vol. 54, no. 83, pp. 11773–11776, 2018.

[28] X. Min, J. Xiao, M. Fang, W. A. Wang, Y. Zhao, Y. Liu and Z. Huang, "Potassium-ion batteries: outlook on present and future technologies," *Energy Environ. Sci.,* vol. 14, no. 4, pp. 2186–2243, 17 02 2021.

[29] K. Cao, H. Liu, W. Li, Q. Han, Z. Zhang, K. Huang, Q. Jing and L. Jiao, "CuO Nanoplates for High-Performance Potassium-Ion Batteries.," *Small,* vol. 15, 1901775, 2019.

[30] L. Xue, H. Gao, W. Zhou, S. Xin, K. Park, Y. Li and J. B. Goodenough, "Liquid K–Na Alloy Anode Enables Dendrite-Free Potassium Batteries," *Adv. Mater.,* vol. 28, no. 43, pp. 9608-9612, 2016.

[31] B. Kishore, G. Venkatesh and N. Munichandraiah, "K2Ti4O9: a promising anode material for potassium ion batteries," *J. Electrochem. Soc.,* vol. 163, no. 13, pp. A2551-A2554, 2016.

[32] V. Gabaudan, L. Monconduit, L. Stievano and R. Berthelot, "Snapshot on negative electrode materials for potassium-ion batteries," *Front. Energy Res.,* vol. 7, no. 46, 00046, 2019.

[33] N. Wang, C. Chu, X. Xu, Y. Du, J. Yang, Z. Bai and S. Dou, "Comprehensive New Insights and Perspectives into Ti-Based Anodes for Next-Generation Alkaline Metal (Na+, K+) Ion Batteries," *Adv. Energy Mater.,* vol. 8, no. 27, 1801888, 2018.

[34] H. Kim, J. C. Kim, M. Bianchini, D. H. Seo, J. Rodriguez-Garcia and G. Ceder, "Recent progress and perspective in electrode materials for K-ion batteries," *Adv. Energy Mater.,* vol. 8, no. 9, 1702384, 2018.

[35] K. Chihara, A. Katogi, K. Kubota and S. Komaba, "KVPO 4 F and KVOPO 4 toward 4 volt-class potassium-ion batteries," *Chem. Commun.,* vol. 53, no. 37, pp. 5208-5211, 2017.

[36] J. Liao, Q. Hu, X. He, J. Mu, J. Wang and C. Chen, "A long lifespan potassium-ion full battery based on KVPO4F cathode and VPO4 anode," *J. Power Sources,* vol. 451, 227739, 2020.

[37] M. Tang, Y. Wu, Y. Chen, C. Jiang, S. Zhu, S. Zhuo and C. Wang, "An organic cathode with high capacities for fast-charge potassium-ion batteries," *J. Mater. Chem. A* , vol. 7, no. 2, pp. 486-492, 2019.

[38] A. Eftekhari, Z. Jian and X. Ji, "Potassium secondary batteries," *ACS Appl. Mater. Interfaces,* vol. 9, no. 5, pp. 4404-4419, 2017.

[39] L. Xue, Y. Li, H. Gao, W. Zhou, X. Lu, W. Kaveevivitchai, A. Manthiram and J. B. Goodenough, "Low-cost high-energy potassium cathode," *J. Am. Chem. Soc.,* vol. 139, no. 6, pp. 2164-2167, 2017.

[40] S. Chong, Y. Chen, Y. Zheng, Q. Tan, C. Shu, Y. Liu and Z. Guo, "Potassium ferrous ferricyanide nanoparticles as a high capacity and ultralong life cathode material for nonaqueous potassium-ion batteries," *J. Mater. Chem. A,* vol. 5, no. 43, pp. 22465-22471, 2017.

[41] C. Zhang, Y. Xu, M. Zhou, L. Liang, H. Dong, M. Wu, Y. Yang and Y. Lei, "Potassium Prussian Blue Nanoparticles: A Low-Cost Cathode Material for Potassium-Ion Batteries," *Adv. Funct. Mater. ,* vol. 27, no. 4, 1604307, 2017.

[42] B. Li, J. Zhao, Z. Zhang, C. Zhao, P. Sun, P. Bai, J. Yang, Z. Zhou and Y. Xu, "Electrolyte-Regulated Solid-Electrolyte Interphase Enables Long Cycle Life Performance in Organic Cathodes for Potassium-Ion Batteries," *Adv. Funct. Mater.,* vol. 29, 1807137, 2019.

[43] Y. Liu, C. Gao, L. Dai, Q. Deng, L. Wang, J. Luo, S. Liu and N. Hu, "The features and progress of electrolyte for potassium ion batteries," *Small,* vol. 16, no. 44, 2004096, 2020.

[44] H. Wang, D. Zhai and F. Kang, "Solid electrolyte interphase (SEI) in potassium ion batteries," *Energy Environ. Sci. ,* vol. 13, no. 12, pp. 4583-4608, 2020.

[45] N. Xiao, W. D. McCulloch and Y. We, "Reversible dendrite-free potassium plating and stripping electrochemistry for potassium secondary batteries," *J. Am. Chem. Soc.,* vol. 139, no. 28, pp. 9475-9478, 2017.

[46] L. Li, S. Zhao, Z. Hu, S. L. Chou and J. Chen, "Developing better ester-and ether-based electrolytes for potassium-ion batteries," *Chem. Sci.,* vol. 12, pp. 2345-2356, 2021.

[47] K. Xu, "Electrolytes and interphases in Li-ion batteries and beyond," *Chem. Rev.,* vol. 114, no. 23, pp. 11503-11618, 2014.

[48] L. J. Krause, W. Lamanna, J. Summerfield, M. Engle, G. Korba, R. Loch and R. Atanasoki, "Corrosion of aluminum at high voltages in non-aqueous electrolytes containing perfluoroalkylsulfonyl imides; new lithium salts for lithium-ion cells," *J. Power Sources,* vol. 68, no. 2, pp. 320-325, 1997.

[49] J. Liao, Q. Hu, Y. Yu, H. Wang, Z. Tang, Z. Wen and C. Chen, "A potassium-rich iron hexacyanoferrate/dipotassium terephthalate@ carbon nanotube composite used for K-ion full-cells with an optimized electrolyte," *J. Mater. Chem. A ,* vol. 5, no. 36, pp. 19017-19024, 2017.

[50] J. M. Macak, H. Tsuchiya, A. Ghicov, K. Yasuda, R. Hahn, S. Bauer and P. Schmuki, "TiO2 nanotubes: Self-organized electrochemical formation, properties and applications," *Current Opinion in Solid State and Materials Science,* vol. 11, no. 1-2, pp. 3-18, 2007.

[51] N. Elgrishi, K. J. Rountree, B. D. McCarthy, E. S. Rountree, T. T. Eisenhart and J. L. Dempsey, "A Practical Beginner's Guide to Cyclic Voltammetry," *Journal of Chemical Education,* vol. 95, no. 2, pp. 197–206, 2018.

[52] A. R. Bredar, A. L. Chown, A. R. Burton and B. H. Farnun, "Electrochemical Impedance Spectroscopy of Metal Oxide Electrodes for Energy Applications," *ACS Applied Energy Materials,* vol. 3, no. 1, pp. 66-98, 2020.

[53] A. Lasia, Electrochemical impedance spectroscopy and its applications, New York: Springer Science+Business Media, 2014.

[54] T. M. Nahir, Impedance Spectroscopy: Theory, Experiment, and Applications, Edited by Evgenij Barsoukov (Texas Instruments Inc.) and J. Ross Macdonald (University of North Carolina, Chapel Hill), Hoboken, NJ: John Wiley & Sons, Inc, 2005.

[55] L. Giorgi, T. Dikonimos, R. Giorgi, F. Buoncore, G. Faggio, G. Messina and N. Lisi, "Electrochemical synthesis of self-organized TiO2 crystalline nanotubes without annealing," *Nanotechnology,* vol. 29, no. 9, 095604, 29 9 2018.

[56] K. Rajiv and K. L. Mittal, "Methods for Assessing Surface Cleanliness," in *Developments in Surface Contamination and Cleaning*, New York, NY, Elsevier, 2019, pp. 23-105.

[57] A. Mayeen, L. K. Shaji, A. K. Nair and N. Kalarikkal, "Morphological characterization of nanomaterials," in *Characterization of Nanomaterials*, Woodhead Publishing, 2018, pp. 335-364.

[58] D. Titus, E. J. J. Samuel and S. M. Roopan, "Chapter 12 - Nanoparticle characterization techniques," in *Green Synthesis, Characterization and Applications of Nanoparticles*, Elsevier, 2019, pp. 303-319.

[59] Z. L. Xu, K. Lim, K. Y. Park, G. Yoon, W. M. Seong and K. Kang, "Engineering solid electrolyte interphase for pseudocapacitive anatase TiO2 anodes in sodium-ion batteries," *Adv. Funct. Mater.,* vol. 28, no. 29, 1802099, 2018.

[60] J. Yang, X. Xiao, W. Gong, L. Zhao, G. Li, K. Jiang, R. Ma, M. H. Rummeli, F. Li, T. Sasaki and F. Geng, "Size-independent fast ion intercalation in two-dimensional Titania Nanosheets for alkali-metal-ion batteries," *Angew. Chem.,* vol. 131, no. 26, pp. 8832-8837, 2019.

[61] Z. Wu, D. Bresser, D. Buchholz, G. A. Giffin, C. R. Castro, A. Ochel and S. Passerini, "Unfolding the mechanism of sodium insertion in anatase TiO2 nanoparticles," *Adv. Energy Mater.,* vol. 5, no. 2, 1401142, 2015.

[62] K. M. Jensen, X. Yang, J. V. Laveda, W. G. Zeier, K. A. See, M. Di Michiel, B. C. Melot, S. A. Corr and S. J. Billinge, "X-ray diffraction computed tomography for structural analysis of electrode materials in batteries," *J. Electrochem. Soc.,* vol. 162, no. 7, A1310, 2015.

[63] L. Fan, S. Chen, R. Ma, J. Wang, L. Wang, Q. Zhang, E. Zhang, Z. Liu and B. Lu, "Ultrastable potassium storage performance realized by highly effective solid electrolyte interphase layer," *Small,* vol. 14, no. 30, 1801806, 2018.

[64] S. S. Zhang, K. Xu and T. R. Jow, "EIS study on the formation of solid electrolyte interface in Li-ion battery," *Electrochim. Acta,* vol. 51, no. 8-9, pp. 1636-1640, 2006.

[65] M. Takeuchi, T. Itoh and H. Nagasaka, "Dielectric properties of sputtered TiO2 films.," *Thin Solid Films,* vol. 51, no. 1, pp. 83-88, 1978.

[66] P. Acevedo-Peña, J. E. Carrera-Crespo, F. González and I. González, "Effect of heat treatment on the crystal phase composition, semiconducting properties and photoelectrocatalytic color removal efficiency of TiO2 nanotubes arrays.," *Electrochim. Acta,* vol. 140, pp. 564-571, 2014.

[67] J. Li, J. Liu, Q. Sun, M. N. Banis, X. Sun and T. K. Sham, "Tracking the effect of sodium insertion/extraction in amorphous and anatase TiO2 nanotubes," *J. Phys. Chem. C,* vol. 121, no. 21, pp. 11773-11782, 2017.

[68] H. He, D. Sun, Y. Tang, H. Wang and M. Shao, "Understanding and improving the initial Coulombic efficiency of high-capacity anode materials for practical sodium ion batteries," *Energy Storage Mater.,* vol. 23, pp. 233-251, 2019.

[69] H. Wang, D. Yu, X. Wang, Z. Niu, M. Chen, L. Cheng , W. Zhou and L. Guo, "Electrolyte Chemistry Enables Simultaneous Stabilization of Potassium Metal and Alloying Anode for Potassium-Ion Batteries," *Angew. Chem. Int. Ed.,* vol. 131, no. 46, pp. 16603-16607, 2019.

[70] D. Wang, L. Liu, X. Sun and T. K. Sham, "Observation of lithiation-induced structural variations in TiO 2 nanotube arrays by X-ray absorption fine structure," *J. Mater. Chem. A,* vol. 3, no. 1, pp. 412-419, 2015.

[71] K. Beltrop, P. Meister, S. Klein, A. Heckmann, M. Grünebaum, H. D. Wiemhöfer, M. Winter and T. Placke, "Does size really matter? New insights into the intercalation

behavior of anions into a graphite-based positive electrode for dual-ion batteries," *Electrochim. Acta,* vol. 209, pp. 44-55, 2016.

[72] M. C. Simoes, K. J. Hughes, D. B. Ingham, L. Ma and M. Pourkashanian, "Estimation of the thermochemical radii and ionic volumes of complex ions. Inorganic chemistry," *Inorg. Chem.,* vol. 56, no. 13, pp. 7566-7573, 2017.

[73] H. Xiong, M. D. Slater, M. Balasubramanian, C. S. Johnson and T. Rajh, "Amorphous TiO2 nanotube anode for rechargeable sodium ion batteries," *J. Phys. Chem. Lett.,* vol. 2, no. 20, pp. 2560-2565, 2011.

[74] K. Yasuda, J. M. Macak, S. Berger, A. Ghicov and P. Schmuki, "Mechanistic aspects of the self-organization process for oxide nanotube formation on valve metals," *J. Electrochem. Soc.,* vol. 154, no. 9, C472, 2007.

[75] F. Bella, A. B. Muñoz-García, G. Meligrana, A. Lamberti, M. Destro, M. Pavone and C. Gerbaldi, "Unveiling the controversial mechanism of reversible Na storage in TiO2 nanotube arrays: Amorphous versus anatase TiO2," *Nano Res.,* vol. 10, no. 8, pp. 2891-2903, 2017.

[76] L. Ling, Y. Bai, Y. Li, Q. Ni, Z. Wang, F. Wu and C. Wu, "Quick activation of nanoporous anatase TiO2 as high-rate and durable anode materials for sodium-ion batteries," *ACS Appl. Mater. Interfaces,* vol. 9, no. 45, pp. 39432-39440, 2017.

[77] K. T. Kim, G. Ali, K. Y. Chung, C. S. Yoon, H. Yashiro, Y. K. Sun, J. Lu, K. Amine and S. T. Myung, "Anatase titania nanorods as an intercalation anode material for rechargeable sodium batteries," *Nano Lett.,* vol. 14, no. 2, pp. 416-422, 2014.

[78] T. Anwar, W. Li, R. U. R. Sagar, F. Nosheen, R. Singh, H. M. Jafri, K. Shehzad and L. Tongxiang, "Cathodic titania nanotube arrays as anode material for lithium-ion batteries," *J. Mater. Sci.,* vol. 52, no. 8, pp. 4323-4332, 2017.

[79] L. Aïnouche, L. Hamadou, A. Kadri, N. Benbrahim and D. Bradai, "Interfacial barrier layer properties of three generations of TiO2 nanotube arrays," *Electrochim. Acta,* vol. 133, pp. 597-609, 2014.

[80] E. Cho, J. Mun, O. B. Chae, O. M. Kwon, H. T. Kim, H. J. Ryu, G. Y. Kim and M. S. Oh, "Corrosion/passivation of aluminum current collector in bis (fluorosulfonyl) imide-based ionic liquid for lithium-ion batteries," *Electrochem. Commun.,* vol. 22, pp. 1-3, 2012.

[81] H. Minowa, Y. Yui, Y. Ono, M. Hayashi, K. Hayashi, R. Kobayashi and K. I. Takahashi, " Characterization of Prussian blue as positive electrode materials for sodium-ion batteries," *Solid State Ionics,* vol. 262, pp. 216-219, 2014.

[82] H. Kim, H. Ji, J. Wang and G. Ceder, "Next-generation cathode materials for non-aqueous potassium-ion batteries," *Trends Chem.,* vol. 1, no. 17, pp. 682-692, 2019.

[83] B. Xie, P. Zuo, L. Wang, J. Wang, H. Huo, M. He, J. Shu, H. Li, S. Lou and G. Yin, "Characterization of Prussian blue as positive electrode materials for sodium-ion batteries," *Solid State Ionics,* vol. 262, pp. 216-219, 2014.

[84] P. Padigi, J. Thiebes, M. Swan, G. Goncher, D. Evans and R. Solanki, "Prussian green: a high rate capacity cathode for potassium ion batteries," *Electrochim. Acta,* vol. 166, pp. 32-39, 2015.

[85] Y. H. Zhu, X. Yang, D. Bao, X. F. Bie, T. Sun, S. Wang, Y. S. Jiang, X. B. Zhang, J. M. Yan and Q. Jiang, "High-energy-density flexible potassium-ion battery based on patterned electrodes," *Joule,* vol. 2, no. 4, pp. 736-746, 2018.

[86] X. Bie, K. Kubota, T. Hosaka, K. Chihara and S. Komaba, "A novel K-ion battery: hexacyanoferrate (II)/graphite cell," *J. Mater. Chem. A,* vol. 5, no. 9, pp. 4325-4330, 2017.

[87] C. Ling, J. Chen and F. Mizuno, "First-principles study of alkali and alkaline earth ion intercalation in iron hexacyanoferrate: the important role of ionic radius," *J. Phys. Chem. C,* vol. 117, no. 41, pp. 21158-21165, 2013.

[88] Y. Mizuno, M. Okubo, E. Hosono, T. Kudo, H. Zhou and K. Oh-ishi, "Suppressed activation energy for interfacial charge transfer of a Prussian blue analog thin film electrode with hydrated ions (Li+, Na+, and Mg2+)," *J. Phys. Chem. C,* vol. 117, no. 21, pp. 10877-10882, 2013.

[89] F. Di Berardino, *"An exploratory study of anodes for potassium batteries", Master of Science thesis,* Torino: Politecnico di Torino, prof. Federico Bella, 2021.

[90] W. Dreyer, J. Jamnick, C. Guhlke, R. Huth, R. Moškon and m. Gaberšček, "The thermodynamic origin of hysteresis in insertion batteries," *Nat. Mater.,* vol. 9, no. 5, pp. 448-453, 2010.

[91] L. Wu, D. Buchholz, D. Bresser, L. G. Chagas and S. Passerini, " Anatase TiO2 nanoparticles for high power sodium-ion anodes," *J. Power Sources,* vol. 251, pp. 379-385, 2014.

[92] D. Yan, C. Yu, X. Zhang, J. Li, J. Li, T. Lu and L. Pan, "Enhanced electrochemical performances of anatase TiO2 nanotubes by synergetic doping of Ni and N for sodium-ion batteries," *Electrochim. Acta,* vol. 254, pp. 130-139, 2017.

[93] X. Wu, Z. Jian, Z. Li and X. Ji, "Prussian white analogues as promising cathode for non-aqueous potassium-ion batteries," *Electrochem. Commun.,* vol. 77, pp. 54-57, 2017.